

**Universidade Federal do Estado do Rio de Janeiro**  
**Centro de Ciências Exatas e Tecnologia**  
**Escola de Informática Aplicada**

Dermatologic Diagnosis through Computer Vision and Pattern Recognition

Juliana Louback

**Mentor**  
Sean Wolfgang Matsui Siqueira Ph.D.

**Rio de Janeiro, RJ - Brazil**  
June 2014

# Dermatologic Diagnosis through Computer Vision and Pattern Recognition

Juliana Louback

Monograph presented at the Escola de Informática Aplicada da Universidade Federal do Estado do Rio de Janeiro (UNIRIO) in order to obtain the title of Bachelor in Information Systems.

---

Sean Wolfgang Matsui Siqueira Ph. D. (UNIRIO)

---

Fernanda Araujo Baião Amorim Ph.D. (UNIRIO)

---

Asterio Kiyoshi Tanaka Ph.D. (UNIRIO)

**Rio de Janeiro, RJ - Brazil**

June 2014

*I would like to dedicate this monograph to prof. Rob Fergus who first introduced me to the field of Computer Vision; and Dr. Jefferson Braga Louback, my father, whose devotion to enabling access to medical care has long inspired my admiration.*

## Acknowledgements

I would like to express my gratitude first and foremost to my mentor, prof. Sean Wolfgang Matsui Siqueira without whose guidance this monograph would never have been completed; prof. Rob Fergus, prof. Richard Staunton and prof. Li Ma who provided invaluable advice regarding the development of the algorithms used; Tom Gibara for his most effective implementation of the Canny Edge Detector and Yuri Pourre for permitting the use of his implementation of the Quick Hull algorithm; my 6 siblings Piero, Daniela, Paula, Natali, Davi and Larissa, some of whom I am certain did all within their power to keep the noise level down to a minimum to avoid hindering my work; my mother Sylvia for her unwavering support and confidence in my ability; Dr. Jefferson B. Louback and Dr. Ricardo Barbosa Lima who contributed with curated images of skin lesions and acted as consultants for the medical aspects of the monograph, which are beyond my domain of knowledge.

## Abstract

This project endeavors to quantify the effectiveness of a selection of computer vision and pattern recognition techniques in the analysis of digital images of skin lesions to diagnose melanoma. In dermatology, the ABCD criteria is a widely known method for the detection of a malignant melanoma. This guide is a set of four identifying traits: Asymmetry; Border irregularity; Color changes; Diameter greater than 6 mm. Over the past decade, various algorithms that examine digital images of skin lesions to detect the presence of malignant melanomas have been developed and tested. Certain algorithms using the analysis of border irregularity alone to provide a diagnosis have presented noteworthy results. The most recent of these was developed by Dr. Richard Staunton of the University of Warwick and Li Ma of the Hangzhou Dianzi University and presents the best results with regards to accuracy and performance. This algorithm uses 13 features based on a set of statistical and geometric irregularity descriptors. The experiment proposed is first to evaluate the images using only a geometric descriptor for border irregularity and compare its effectiveness to Ma and Staunton's multi-descriptor analysis. Next, a metric is developed to represent the remaining 3 categories of the ABCD melanoma diagnosis criteria to be used in conjunction with the Border Irregularity metric. and increase levels of accuracy. A second round of evaluations is performed to ascertain the influence of the additional metrics. The algorithms are run on a labeled dataset of 70 images and the specificity, the number of accurately diagnosed images of melanoma, is calculated. Sensitivity is of lesser importance as incorrectly classifying a non-malignant lesion as malignant presents less critical consequences as overlooking a malignant lesion. However, in both cases, sensitivity is also taken into consideration in the final evaluation. In conclusion, a practical application of these techniques is explored with the intent of providing solutions to the prevalent issue of limited access to medical care. The process, maturation and findings of the undertaking are detailed in this monograph.

**Keywords:** Computer Vision, ABCD Criteria, Pattern Recognition.

## Index

|                                       |    |
|---------------------------------------|----|
| 1. INTRODUCTION                       |    |
| 1.1 The Scope of Analysis.....        | 9  |
| 1.2 Monograph Structure .....         | 11 |
| 2. FUNDAMENTALS                       |    |
| 2.1 ABCD Criteria.....                | 12 |
| 2.2 Related Work.....                 | 15 |
| 3. APPROACH.....                      | 18 |
| 4. REIMPLEMENTATION                   |    |
| 4.1 Staunton and Ma's algorithm.....  | 20 |
| 5. IMPLEMENTATION                     |    |
| 5.1 Canny Edge Detector.....          | 28 |
| 5.2 AB*CD Metrics                     |    |
| 5.2.1 Asymmetry metric.....           | 32 |
| 5.2.2 Border irregularity metric..... | 35 |
| 5.2.3 Color change metric.....        | 37 |
| 5.2.4 Diameter size.....              | 38 |
| 6. ANALYSIS                           |    |
| 6.1 Pre-processing.....               | 39 |
| 6.2 Dataset.....                      | 39 |
| 6.3 Data Analysis.....                | 40 |
| 7. CONCLUSION.....                    | 43 |

## List of Tables

|   |    |
|---|----|
| Table 1 - Comparison of classification performances.....                  | 17 |
| Table 2 - Summary of Key ABCD(E) Sensitivity and Specificity Studies..... | 18 |
| Table 3 - Final feature selection.....                                    | 27 |
| Table 4 - BP Neural Net and Naïve Bayes performance.....                  | 40 |
| Table 5 - Abbreviation Glossary.....                                      | 41 |
| Table 6 - Comparison: StauntonMa + A + C with BP Neural Net.....          | 42 |
| Table 7 - Comparison: StauntonMa + A + C with Naïve Bayes.....            | 42 |

## List of Figures

|  |    |
|--|----|
| Figure 1 - Mean dermatologist density among US counties.....                 | 10 |
| Figure 2 - Asymmetry: Malignant and benign example.....                      | 12 |
| Figure 3 - Border Irregularity: Malignant and benign example.....            | 13 |
| Figure 4 - Color Variegation: Malignant and benign example.....              | 13 |
| Figure 5 - Diameter Size: Malignant example.....                             | 14 |
| Figure 6 - Wavelet decomposition tree.....                                   | 21 |
| Figure 7 - Contours after wavelet reconstruction.....                        | 24 |
| Figure 8 - Comparison of optimal and Gaussian operator.....                  | 28 |
| Figure 9 - Threshold performance comparison.....                             | 31 |
| Figure 10 - Threshold performance on image of melanoma.....                  | 31 |
| Figure 11 - Polygon containing the skin lesion: Melanoma and Neoplasm.....   | 34 |
| Figure 12 - Summary of Symmetry Detector results: Melanoma and Neoplasm..... | 35 |
| Figure 13 - Comparison of simple border irregularity metric.....             | 36 |
| Figure 14 - Comparison of Melanoma and Neoplasm Average Delta-E.....         | 37 |
| Figure 15 - Comparison of $B^*$ metric precision.....                        | 41 |

## 1. INTRODUCTION

The first chapter of this monograph provides a high-level understanding of the motivation behind this research. The scope of analysis is defined in order to demonstrate the importance and potential value which may be added followed by a brief description of the structure of the monograph to facilitate comprehension.

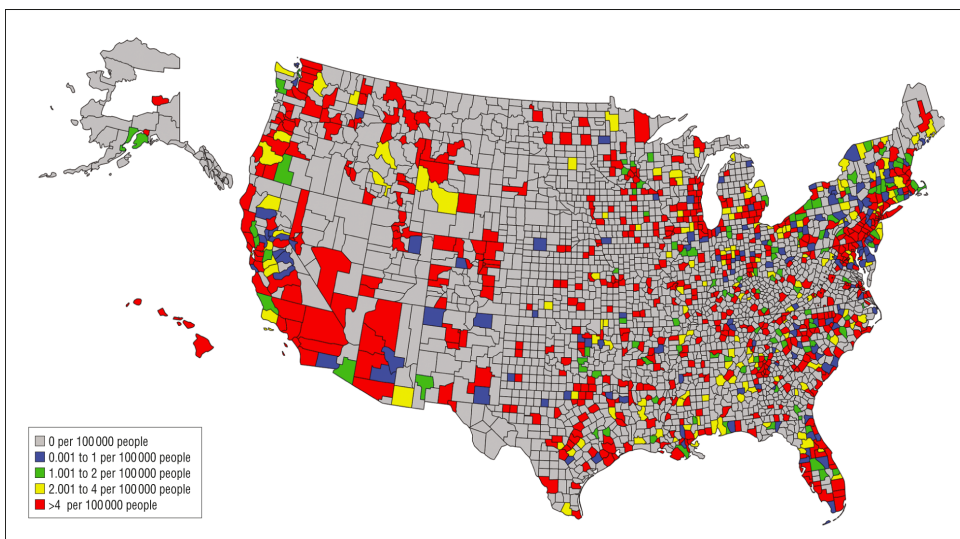
### 1.1 The Scope of Analysis

There is a noted undersupply of dermatologic services worldwide, common to both developing and developed countries. The effects of such a deficit in the workforce is clearly shown in the excessive mean wait times for appointment availability; it was recently discovered that a patient must schedule a dermatologic consult an average of 33 days in advance in the United States [13] and 26 days in advance in Brazil [21].

Estimates of the current number of practicing dermatologists range from 8,000 to 8,5000 in the United States and approximately 6,000 in Brazil. This is a pitifully inadequate number of professionals to cater to the 300 million americans and 200 million brazilians. Researchers from the Case Western Reserve University and Yale University performed a study that showed the direct correlation between dermatologist density and melanoma mortality rates [2]. This finding is already significant in countries like the United States and Brazil where there is an estimated ratio of 35,000 people per dermatologist and even more severe in countries like South Africa with 3 to 4 million people per dermatologist [19].

Dermatology specialists are mainly based in capitals and major cities, limiting greatly the access to a dermatologist (*See Figure 1*). Technology has previously been applied to other fields to overcome geographical barriers; this project evaluates the efficiency and effectiveness of a series of computerized methods that may be applied to the dermatologic diagnosis process, in an effort to assuage this disequilibrium in supply and demand.

Figure 1 - Mean dermatologist density among US counties, 2002-2006



Source: ANEJA, S; ANEJA, S; BORDEAUX J.S [2]

In the field of dermatology, the vast majority of medical cases are diagnosed visually, as the affected regions are at least partially superficial. According to CDC's National Ambulatory Medical Care Survey in 2009, the top 5 reasons given by patients for visiting dermatologists were actinic and seborrheic keratosis, benign neoplasm, acne, malignant neoplasms and contact dermatitis and other eczema. These conditions account for near 80% of medical consults. Of the 5 listed, 4 can be diagnosed through a visual examination.

The National Cancer Institute defines a neoplasm as an abnormal mass of tissue that results when cells divide more than they should or do not die when they should. A neoplasm can also be called a tumor and may be benign or malignant. Melanoma is a malignant neoplasm that begins in melanocytes commonly on skin but may also begin in other pigmented tissues such as in the eye or in the intestines. The scope of this project will be limited to skin melanoma diagnosis through digital image analysis, using binary classification algorithms with melanoma/non-melanoma as prediction categories.

Within the ambit of neoplasm diagnosis, there are certainly more options than melanoma and non-melanoma. Among the malignant neoplasms there are non-melanoma skin cancers, consisting primarily of basal cell carcinomas and squamous cell carcinomas [28]. Multinomial classification could be employed to include these varieties of neoplasms in the analysis performed, yet would add significant

complexity. On that account, it was decided that a more conservative approach would be most adequate for the initial stages of this study, limiting the classifier algorithm to two categories. As melanomas are more commonly fatal than non-melanoma malignant neoplasms [28], melanoma diagnosis was defined as the the focus of the research.

Skin melanoma may be diagnosed through a visual examination performed by a dermatologist. The definitive diagnosis is usually rendered on pathologic evaluation of a lesional skin biopsy specimen [27]. The potential malignancy is recognized during the initial (visual) examination, following which a biopsy is performed to confirm the prognosis. As such, although image analysis systems are not to be relied upon for a complete diagnosis, they may be a viable solution to perform a triage and prioritize examinations.

## **1.2 Monograph Structure**

The monograph is organized into 7 chapters, these being Introduction, Fundamentals, Approach, Reimplementation, Implementation, Analysis and Conclusion. The first chapter describes the domain of the issue, that of automated melanoma detection, as well as a high level description of the solution proposed. The introductory chapter also provides a basic explanation of the medical terms employed. Fundamentals discusses previous studies in related fields and how prior findings will be included in this monograph. Approach details the solution developed, describing the components and logic pertaining to the image analysis system. Reimplementation describes Staunton and Ma's Border Irregularity analysis algorithm and the process of reconstructing it's code. The Implementation chapter documents the development of three additional algorithms to be used in conjunction with Staunton and Ma's. Analysis outlines the execution of the image analysis system, resulting in a dataset to be used in the classifier system as well as the intermediate results obtained during testing. Conclusion will summarize the performance of the classifier system, its findings and ongoing work.

## 2. FUNDAMENTALS

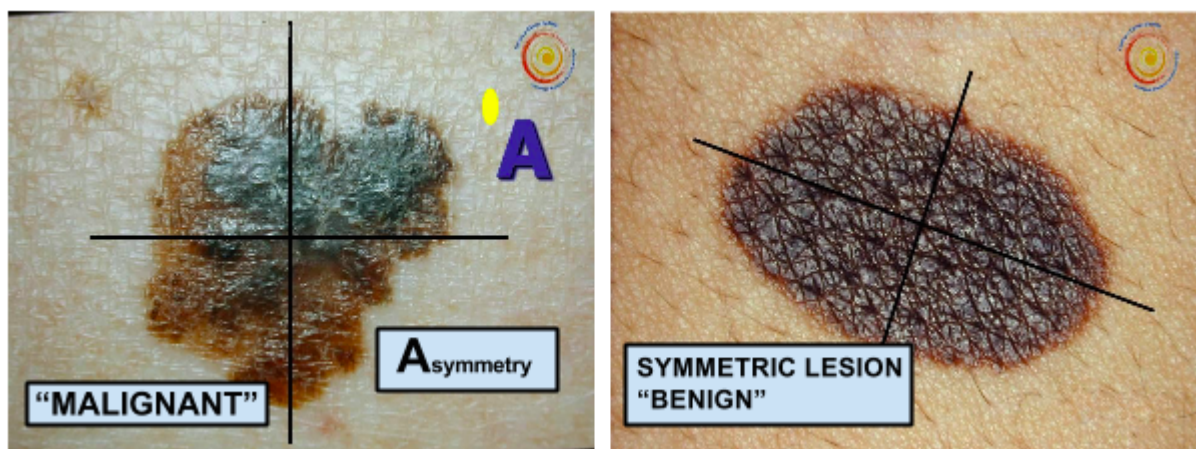
The following chapter details the identifying traits used to detect melanoma in a visual examination and a description of previous studies related to the employment computer vision methods and algorithms for dermatologic diagnosis.

### 2.1 ABCD Criteria

The ABCD acronym was first coined in the article *Early Detection of Malignant Melanoma: The Role of Physician Examination and Self-Examination of the Skin* [7] written by Dr. Robert Friedman, Dr. Darrell Rigel and Dr. Alfred Kopf of the New York University School of Medicine in 1985. This article was prepared in conjunction with the Task Force on Preventive Dermatology of the American Academy of Dermatology and the American Cancer Society; the ABCD Criteria was meant to be used by both the lay public and health professionals to assist in the early detection of melanoma and consequently increase survival rates [7]. ABCD stands for Asymmetry, Border Irregularity, Color variegation, and Diameter generally greater than six mm [7].

#### Asymmetry

Figure 2 - Asymmetry: Malignant and benign example

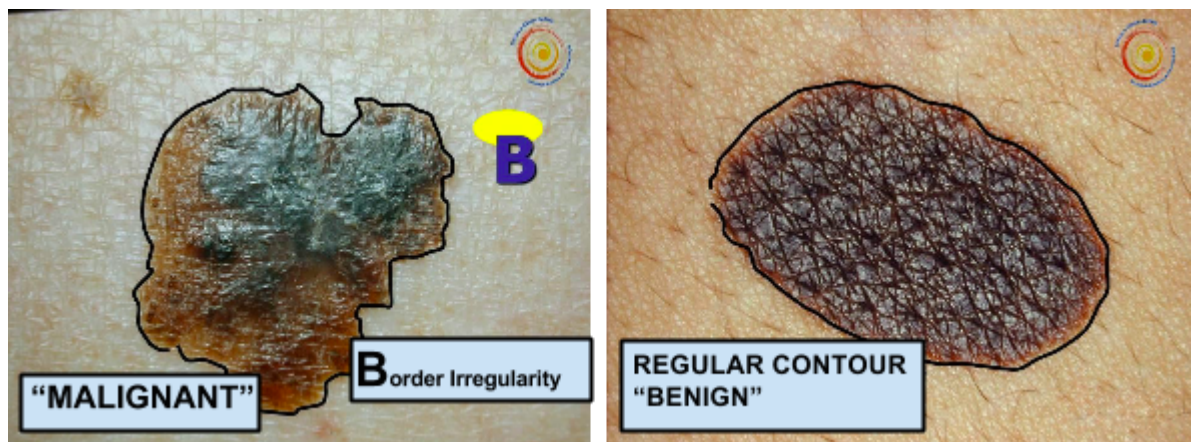


Source: prof. Ricardo Barbosa Lima of UNIRIO

"Unlike benign pigmented lesions, which are generally round and symmetrical, early malignant melanomas are usually asymmetrical" [7] (Figure 2)

## Border Irregularity

Figure 3 - Border Irregularity: Malignant and benign example

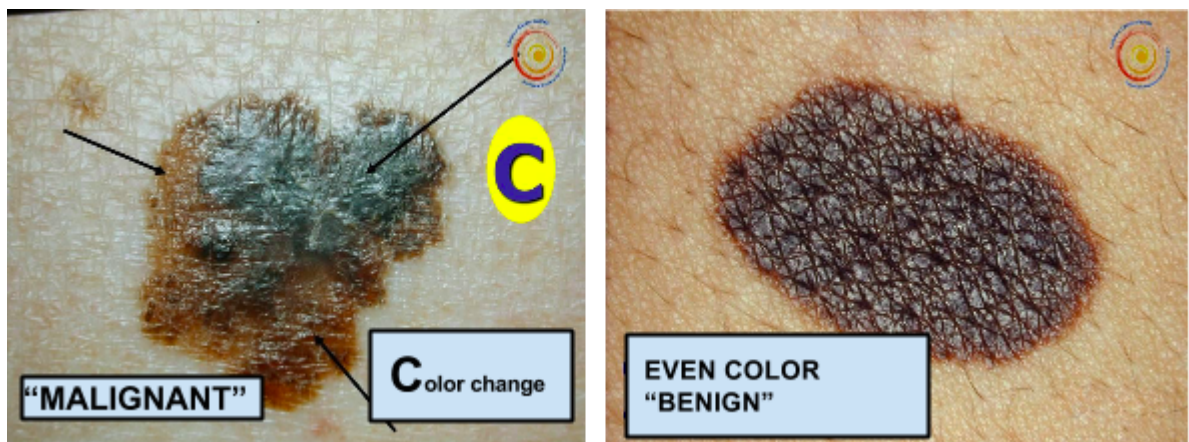


Source: prof. Ricardo Barbosa Lima of UNIRIO

"Unlike benign pigmented lesions, which generally have regular margins, the borders of early malignant melanomas are usually irregular." [7] (Figure 3)

## Color Variegation

Figure 4 - Color Variegation: Malignant and benign example

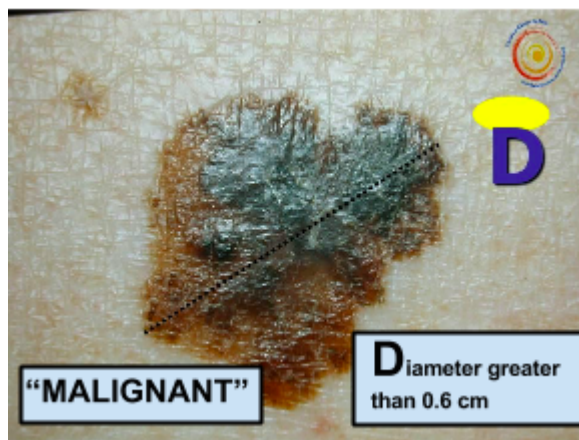


Source: prof. Ricardo Barbosa Lima of UNIRIO

"Unlike benign pigmented lesions, which are generally uniform in color, macular malignant melanomas are variegated, ranging from various hues of tan and brown to black, and sometimes intermingled with red and white." [7] (Figure 4)

## Diameter Size

Figure 5 - Diameter size: Malignant example



Source: prof. Ricardo Barbosa Lima of UNIRIO

"Unlike most benign pigmented lesions, which generally have diameters less than six mm, the diameters of macular malignant melanomas when first identified are often more than six mm." [7] (Figure 5)

It is possible that the fourth trait, 'Diameter greater than 6 mm', may not be as symptomatic as the previous 3 traits. A study performed in 2004 by Dr. Friedman, Dr. Rigel, and Dr. Kopf and other colleagues of the New York University School of Medicine and the Sydney Melanoma Unit suggested a reexamination of the ABCD criteria in view of data attesting to the existence of melanoma with a diameter smaller than 6 mm [1]. Although the conclusion reached was that the available data did not support a lowering of the 6mm threshold, the study emphasizes the need to use the ABCD traits in conjunction as there are cases of small-diameter melanomas.

During the same study by Kopf and his colleagues, detailed in the article *Early Diagnosis of Cutaneous Melanoma: Revisiting the ABCD Criteria* [1] it was concluded that an additional criterion 'E' should be added to the acronym, representing the evolution of pigmented lesions. It is said that "Physicians and patients (...) should be attentive to changes (evolving) of size, shape, symptoms (itching, tenderness), surface (especially bleeding), and shades of color." [1] However, this additional criterion cannot be well represented by a digital image and as such is not included in this experiment.

## 2.2 Related Work

In dermatology, the ABCD guide is a widely known method for the identification of a malignant melanoma [23]. This guide is a set of 4 traits common to malignant melanomas: Asymmetry; Border irregularity; Color variegation; Diameter greater than 6 mm. Symmetry in medical imaging has played an important role in contributing to diagnosis in other fields of medicine. An example of this is measuring asymmetry on mandibles from children with cleft lip and palate and children with plagiocephaly syndrome [10], measuring the asymmetry of the hippocampi to classify schizophrenic patients [10] and using the asymmetry principle in the detection of breast tumors [14].

Extensive research has been performed regarding the digital analysis of border irregularity in relation to melanoma diagnosis. Some of these studies indicate that the diagnosis of malignant melanomas can be based on the analysis of the shape of the lesion alone [15]. Many of said studies which present most noteworthy results make use of Wavelet Transform Analysis.

The term ‘wavelet’ (originally in French, ‘ondelettes’) was first coined in 1982 by the French geophysicist Jean Morlet [22], one of the pioneers in Wavelet Analysis. Morlet sought an alternative to the short time Fourier Transform [6] which is a modification of the Fourier transform to permit the analysis of non-stationary signals. Assuming a time-domain signal as the raw signal, a Fourier transform could be used to obtain the Frequency Spectrum. The Fourier Transform contains no information with regard to time, ergo the need for the short time Fourier Transform for a non-stationary signal. The short time Fourier Transform performs sequential Fourier Transforms on segments of the signal which are (near) stationary.

The disadvantage of the short time Fourier transform lies in the necessary sacrifice of either good time resolution or good frequency resolution according to the window used in the kernel function. To gain good time resolution in the high-frequency components as well as good frequency resolution in low-frequency components in a single transform, Morlet proposed an alternate method for generating the transform functions. In sum, instead of using a window of changeable width to perform a Fourier Transform on a time interval of the signal, Morlet took a windowed cosine wave whose width was shifted to adjust to low or high frequencies and shifted these functions in time

as well [6]. As a result, the transform functions relied on two parameters: the time location and scale, which represents the frequency. Since then, the basis Wavelet theory has been built upon by a series of scientist who have explored its applications in a variety of fields.

There are two main trends in the use of Wavelet Transforms [12], the Continuous Wavelet Transforms and the Discrete Wavelet Transforms. The Continuous Wavelet Transforms (CWT) consists of an analysis window (function) of varying scale being shifted not only in scale but in time, obtaining the signal product and integrating over all times. In the Discrete Wavelet Transform (DWT) low and high pass filters are used to analyze low and high pass frequencies, respectively, removing redundancy present in the CWT. The CWT's redundancy does have a purpose, emphasizing traits and adding readability. The DWT reduced computational time due to reduced redundancy may be the cause of its greater popularity among engineers [12].

A study performed by K.M. Clawson of the University of Ulster uses the Harmonic Wavelet Transform to analyze lesion border irregularity, claiming maximum classification accuracy of 93.3% with 80% sensitivity [5] when tested on 30 cutaneous lesions. The Harmonic Wavelet Transform was developed by David Newman in 1993 [24]. This name may be derived from its frequency resolution, "confined exactly to an octave band so that it is compact in the frequency domain" [24]. However, this fixed resolution throughout the frequency band inhibits the separation of signal components [17] which in turn hinders the distinction of structural and textural irregularities. It is the structural irregularity that has clinical importance for melanoma diagnosis [17]. In 2012, Li Ma of the Hangzhou Dianzi University and Richard C. Staunton of the University of Warwick circumvented this difficulty by using a Discrete Wavelet Transform to single out the structural components [17]. Their study involved 134 images of skin lesions; of these 72 were of melanomas and 62 of moles. The most significant distinction between melanomas and moles is that moles are benign neoplasms whereas melanomas are malignant neoplasms. The algorithm could be summarized as a two-step procedure: multi-scale wavelet decomposition of the extracted contour followed by the selection of significant sub-bands.

Wavelet decomposition was used to extract the structure from the contour which

were then modeled as signatures with scale normalization to give position and frequency resolution invariance. Energy distributions among different wavelet sub-bands were then analyzed to extract those with significant levels and differences to enable maximum discrimination. A set of statistical and geometric irregularity descriptors were applied at each of the significant sub-bands, followed by an effectiveness evaluation to select which descriptors contribute to an accurate diagnosis. The effectiveness of the descriptors was measured using the Hausdorff distance between sets of data from melanoma and mole contours. The best descriptor outputs were input to a back projection neural network to construct a combined classifier system. This algorithm will be described in greater detail in the implementation chapter of the monograph.

Li and Staunton's optimum combination resulted in 90% specificity and 83% sensitivity, similar to Clawson's findings. These results were obtained from a small data set consisting of 18 images, 9 of which were of melanomas and 9 of moles. With a larger training set of 67 images (31 moles and 36 melanomas), these numbers fell to 83% sensitivity and 74% specificity, which signifies that a greater number of non-malignant moles would be classified as melanomas.

Table 1 - Comparison of classification performances

| Scheme  | Specialty | Sensitivity | Area of ROC |
|---|-----------|-------------|-------------|
| Single scale features with small sample set         | 0.64566   | 0.69444     | 0.69534     |
| Single scale features with large sample set         | 0.87903   | 0.55556     | 0.75179     |
| Original multi-scale features with small sample set | 0.83871   | 0.69444     | 0.81541     |
| Original multi-scale features with large sample set | 0.80645   | 0.69444     | 0.81989     |
| Selected multi-scale features with large sample set | 0.74194   | 0.83333     | 0.83333     |
| Selected multi-scale features with small sample set | 0.90323   | 0.83333     | 0.89068     |

Source: MA, L.; STAUNTON, R.C. [17]

These findings are incredibly significant given the high levels of accuracy and reduced computational cost. It is of interest to analyse this algorithm in conjunction with remaining three features of the ABCD criteria: asymmetry, color change and diameter size.

### 3. APPROACH

This study implemented and evaluated a multi feature image analysis system in an effort to gauge the effectiveness of its employment in melanoma diagnosis. It became necessary to first identify the significance of each feature in the classification of skin lesions to determine what combination of features provide the most accurate results.

Li Ma and Richard C. Staunton generously agreed to the inclusion of their algorithm in this experiment. However, the original software for the algorithm detailed in the article *Analysis of the contour structural irregularity of skin lesions using wavelet decomposition* [17] could not be recovered. To circumvent this contrempts, the algorithm was reimplemented in consultation with Ma and Staunton as part of the study.

Our approach is divided into two parts; the first is Ma and Staunton's algorithm, which uses border irregularity to determine malignancy. Border irregularity is one of four identifying traits used in the diagnosis of melanoma. Studies have shown that accuracy levels vary according to the traits included in performing diagnosis, both singly and in combination. Table 2 summarizes the findings of research led by L. Thomas in 1998 [28], displaying distinct fluctuations in performance when combining multiple criteria. Therefore the second part of the system consists of three algorithms to formulate additional metrics, these being Asymmetry, Color change and a simple geometric border irregularity descriptor.

Table 2 - Summary of Key ABCD(E) Sensitivity and Specificity Studies

| Source                                   | Total No. of Lesions | No. of Melanomas | Criteria Tested              | Sensitivity, %       | Specificity, %     |
|--|----------------------|------------------|------------------------------|----------------------|--------------------|
| Thomas et al, <sup>4</sup> 1998*         | 1140                 | 460              | A                            | 57                   | 72                 |
|  |                      |                  | B                            | 57                   | 71                 |
|  |                      |                  | C                            | 65                   | 59                 |
|  |                      |                  | D                            | 90                   | 63                 |
|  |                      |                  | E                            | 84                   | 90                 |
|  |                      |                  | ≥1 Criterion                 | 97                   | 36                 |
|  |                      |                  | ≥2 Criteria                  | 89                   | 65                 |
|  |                      |                  | ≥3 Criteria                  | 66                   | 80                 |
|  |                      |                  | ≥4 Criteria                  | 54                   | 94                 |
|  |                      |                  | All 5 criteria               | 43                   | 100                |
|  |                      |                  | BCD criteria applied jointly | 100 (95% CI, 54-100) | 98 (95% CI, 95-99) |
| McGovern and Litaker, <sup>10</sup> 1992 | 192                  | 6                |                              |                      |                    |
| Healsmith et al, <sup>3</sup> 1994†      | 165                  | 65               | ≥1 of the ABCDEs             | 92 (95% CI, 82-96)   | Not reported       |

Source: Thomas, L. et al. [28]

Staunton and Ma's algorithm uses 13 features based on a set of statistical and geometric border irregularity descriptors. In addition, this algorithm extracts the structural component of the lesion from the raw image data, eliminating the misleading textural component. The simple geometric descriptor is compared with Ma and Staunton's algorithm to measure the added accuracy of the 13 features used as well as the impact of refining the raw data. Subsequently the two descriptors for Asymmetry and Color change are included in a combined algorithm. As stated by Kopf and his colleagues [1], "It should be emphasized that not all melanomas have all 4 ABCD features. It is the combination of features (eg, ABC, A+C, and the like) that render cutaneous lesions most suspicious for early melanoma." If this is true of in-person examinations performed by a specialist, it may also be implied of computer vision analysis.

Combining the 13 features in Staunton and Ma's algorithm and the 3 additional metrics, a total of 16 features are attributed to each image of a skin lesion, recorded in the data set which is run through a Back Propagation Neural Network to classify each instance as melanoma or non-melanoma. The back propagation (BP) neural network algorithm is a multi-layer feedforward network trained according to error back propagation algorithm and is one of the most widely applied neural network models [11]. This model was used in the development of Ma and Staunton's algorithm and will continue to be used to maintain consistency. The algorithm is measured for sensitivity and specificity levels in addition to overall accuracy.

Sensitivity is given a higher priority than specificity, as the correct identification of a malignant or potentially malignant tumor is of greater consequence than a false positive diagnosis, within reasonable levels. Of course, the inconvenience of a false positive diagnosis is by no means irrelevant, so despite specificity being a secondary priority, this category of performance is still carefully observed. As achieving 100% accuracy is an unrealistic expectation and the biopsy a requirement for a definitive diagnosis [27], specialist confirmation remains necessary. This project seeks to contribute to the discussion of whether it is advantageous to incorporate computer vision algorithms to current traditional diagnosis methods.

## 4. REIMPLEMENTATION

As the code for Staunton and Ma's algorithm was not recovered, it became necessary to re implement the algorithm to enable its inclusion in this experiment. The reimplementaion of Ma and Staunton's Border Irregularity algorithm is described, in accordance to the procedure detailed in Staunton and Ma's article *Analysis of the contour structural irregularity of skin lesions using wavelet decomposition [17]*.

### 4.1 Staunton and Ma's Algorithm

Li Ma and Richard C. Staunton of the Hangzhou Dianzi University and Warwick University [17] developed an algorithm to analyze skin lesion border irregularity using multi-scale wavelet decomposition. As the code for the algorithm was not recovered, it was necessary to re-implement it so as to include it in this study. The code was originally written in Matlab, a high-level technical computing language and interactive environment for algorithm development. However, due to budget limitations the algorithm was re-implemented in Octave, an open source alternative comparable to and generally compatible with Matlab. The algorithm is roughly divided into two phases: Wavelet decomposition of a lesion contour and Sub-band descriptions of contour structural components. Following is a summarized and commented description of the algorithm extracted from the article *Analysis of the contour structural irregularity of skin lesions using wavelet decomposition [17]*.

#### 1. Wavelet decomposition

##### 1.1. Represent the contour in 1D signal

The contour of a skin lesion in an image is described by the points  $C = \{x_1, y_1, x_2, y_2, \dots, x_N, y_N\}$ . [These points were obtained using a Canny edge detector function.] To represent this 2D data as 1D, the contour is modeled as a signature  $C_r = \{r_1, r_2, \dots, r_N\}$  where the radial distance from the geometric center  $r_i = \sqrt{(x_i - x')^2 + (y_i - y')^2}$ ,  $i = 1, 2, \dots, n$  and  $(x', y')$  is the coordinate of the geometric center of the closed contour.

##### 1.2 Scale normalization

It was noted that many moles have a shorter contour for a given nominal area than do

melanomas. Together with size variability between the samples in the database, this can lead to variations in estimated frequency and resolution in the frequency domain. Scale normalization is required to enable a comparison between moles and melanomas in this domain. The proposed normalization was modified to give radius:

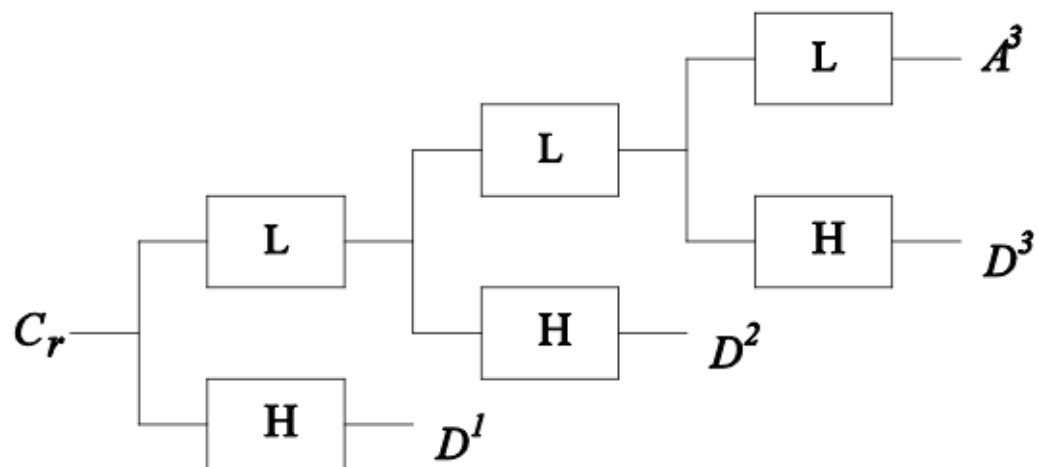
$$r'_i = \begin{cases} r\left(\left\lceil i \frac{n}{N} \right\rceil\right) + \mu_1 - \mu_2 & r(i) < T \\ r\left(\left\lceil i \frac{n}{N} \right\rceil\right) & \text{otherwise} \end{cases} \quad i=1,2,\dots,N$$

Where  $i$  is an integer used to resample the contour points with a spacing distance of  $(n/N)$  and the ceiling function  $\lceil \cdot \rceil$  is used to produce an integer index to  $r$ . The values  $\mu_1$  and  $\mu_2$  are the averaged radial distances of all the melanomas and benign moles respectively in the data base.  $T$  is a threshold.

### 1.3 Wavelet decomposition

Wavelet decomposition is a powerful tool for multi-scale signal analysis. By using a pair of low-pass and high-pass filters [the lesion contour signature] is decomposed into approximation and detail coefficients with the approximations feeding into the next level of decomposition, and thus creating a decomposition tree. The tree structure of such a 1D wavelet decomposition is shown in Figure 6.

Figure 6 - Wavelet decomposition tree



Source: MA, L.; STAUNTON, R.C. [17]

The approximate and detail coefficients (see section 2.2) at scale  $i$  are given by  $A_i = \{a_1^i, a_2^i, \dots, a_M^i\}$  and  $D_i = \{d_1^i, d_2^i, \dots, d_M^i\}$  respectively where  $M = N/2^i$ . It is important to recall that the Discrete Wavelet Analysis uses windowed cosine wave whose width is successively modified. The width, also known as compression of said wave is represented by a scale [6]. The smaller the scale, the more narrow the wave ergo the higher the frequency. The inverse is also true; the greater the scale, the wider the wave ergo the lower the frequency. As the scale increases, the approximate coefficients are further decomposed into low and high frequency components at the next higher scale. Generally the textural components of a contour occupy the lower scale, higher frequency bands, with the energy distributed evenly between bands to give a relatively small total energy within each. However the structural components generally have a larger energy and occupy the lower frequency bands. By using wavelet decomposition to level  $s$ , an original contour signature  $C$  is transformed to a series of sub-band signals  $A^s, D^s, D^{s-1}, \dots, D^1$  covering the whole signal frequency space at  $[0, 1/2^s f_{max}], [1/2^s f_{max}, 1/2^{s-1} f_{max}], \dots, [1/2^1 f_{max}, 1/2^0 f_{max}]$ . This represents a concatenation of the frequency bands from the lowest to the highest. The task is to identify at which decomposition levels the structural components of a lesion contour can be extracted and which sub-bands in the frequency domain are significant for distinguishing moles and melanomas.

## *2. Sub-band descriptions of contour structural components*

The Discrete Wavelet Transform was selected for use over the Fast Fourier Transform because it presents the capability of confining signal components to dyadically increasing width frequency bands with different resolutions. This enables the distinction between structural and textural components, an essential factor in Staunton and Ma's algorithm.

### *2.1 Significant sub-band selection*

To obtain just the contour's structural components ignoring the less relevant textural components, several lower frequency sub-bands need to be identified from which to reconstruct that portion of the original contour using both multi-scale approximate and detail coefficients. The evaluation of the significant sub-band range was accomplished by performing a Hausdorff distribution analysis between each of the sample sets at each level of wavelet decomposition. When analyzing the

decomposition of a contour signal, the total energy at any decomposition level indicates the significance of that sub-band frequency to the original signal. The energy of a wavelet sub-band  $D_j$  is defined as

$$E_j = \sum_i (D_j^i)^2 \quad j = 1, 2, \dots, n$$

### *2.2 Procedure for investigating significant sub-band selection*

An algorithm was developed to identify those sub-bands which enabled the largest discrimination between moles and melanomas. This was done with a set of  $p$  benign mole contours and a set of  $q$  melanoma contours

Step 1: For a preset maximum level of wavelet decomposition  $n$ , calculate the wavelet energy for every contour from the set of moles and melanomas. Then calculate the energy of each sub-band [obtained from the wavelet decomposition to level  $n$ ].

Step 2: Form energy sets from the individual energies calculated for each transformed benign mole and melanoma contour at each sub-band.

Step 3. Compute the Hausdorff Distance value between energy sets of moles  $E_b$  and melanomas  $E_m$  for each band. This measures the discrimination between the two classes for each sub-band.

Step 4. Plot the distribution of the Hausdorff Distance with respect to each sub-band. The sub-bands with the highest HD are considered as the most significant and used in the final classification.

### *2.3 Extraction of the structural component of a lesion contour*

Based on the theory of wavelet reconstruction, the structural component of a lesion contour is given by combining the significant coefficient groups from  $A^s$ ,  $D^s$ ,  $D^{s-1}$ , ...  $D^1$  where the original decomposition was stopped at level  $s$ . The decomposed detail sub-bands need to be divided into high-scale (low-frequency) and low-scale (high-frequency) groups using a threshold  $s_t$  so that:

$$C_s = \{A^s + D^s + D^{s-1} + \dots + D^{st}\}$$

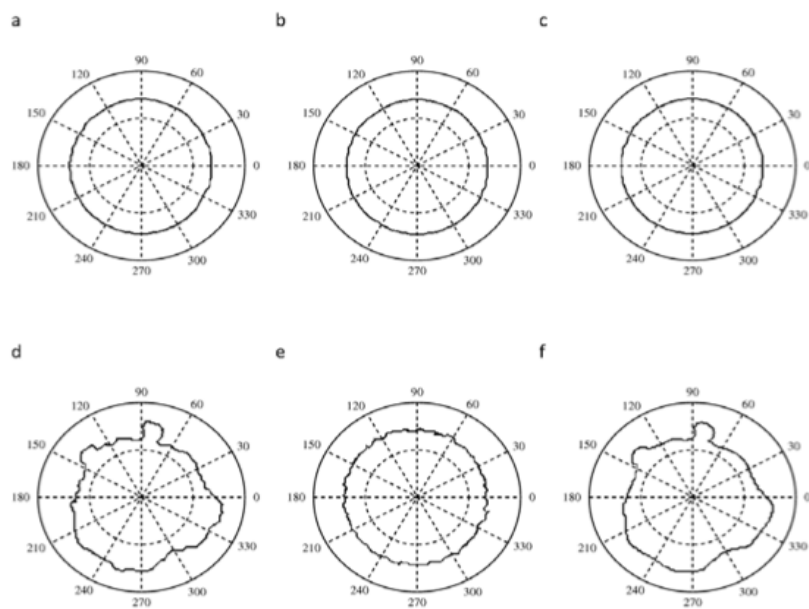
$$C_t = \{D^{st-1} + D^{st-2} + \dots + D^1\}$$

Where  $C_s$  contains lower-frequency information and represents the structural component of the contour, and  $C_t$  contains higher-frequency information and represents the textural component. Choosing both  $s$  and  $s_t$  are difficult tasks, as a large  $s$  generates many narrow sub-bands close to zero frequency. Although these

will contain structural information that will be relatively free of textural irregularity, there is an extra cost in increased computational complexity. A small  $s$  can lead to structural contours contaminated with textural irregularity. The value of  $s_t$  chosen is crucial to obtain useful structural and textural contour information. The significant sub-band selection process described in Section 2.2 was run on the test data which lead to the straightforward selection of a single, general value for  $s_t$ . The frequency bands that contained significant discrimination information were sub-bands  $D^6$  to  $D^9$ , and as such were selected as the significant levels.

It is simple to reconstruct the structural components of the contour after the significant levels in the wavelet decomposition stack have been determined. Figure 7 shows the extracted contours of a mole (a,b,c) and a melanoma (d,e,f), where Figure 7 a) and d) are the original contours, Figure 7 b) and e) are the corresponding contours reconstructed from  $A^9$  and  $D^1$  to  $D^5$ . The approximation coefficient,  $A^9$  has been included to give the basic structure of the contour onto which the more complex textural part has been superimposed. Figure 7 c) and f) are reconstructed from  $A^9$  and  $D^6$  to  $D^9$  ( $s = 9$ ,  $s_t = 6$ ), that is the boundaries representing the structural portion of the original lesion. With the textural information removed, these have the property of the highest discrimination between different lesion classes. In the remainder of the monograph these significant sub-bands will be referred to as the structural sub-bands.

Figure 7 - Contours after wavelet reconstruction



Source: MA, L.; STAUNTON, R.C. [17]

Observing Figure 7, one can easily note the striking difference in discrimination based on textural and structural components. The contours in b) and e) reconstructed from the textural components of the mole and melanoma respectively present an almost imperceptible difference and would add very little to a classification system. In contrast, the contours c) and f) which were reconstructed from the structural components are clearly distinctive. As the significant sub-band selection was performed during Ma and Staunton's study, leading to the selection of a single value for  $s_t$ , with the approval of Li Ma, this phase of the algorithm was bypassed; the re-implementation uses the selected  $s_t$  value directly.

Once the significant sub-bands were identified, it was possible to calculate the series of border irregularity measures the algorithm is comprised of. Ma and Staunton used 7 different measures, these being either statistical or geometric based [17]. The measures and their respective formulas are listed below as described in Ma and Staunton's article:

### 3.1 Statistical measures

The following features related to contour irregularity were defined:

(1) The mean of the energy of  $D^j$  at each significant level, given by:

$$\mu = \left( \sum_{i=1}^N d_i \right) / N \text{ where } d_i \text{ is the } i\text{th component of } D^j.$$

$$(2) \text{ Entropy of wavelet energy, } w_j = - \sum_{i=1}^N p_i^j \log(p_i^j)$$

where  $p_i^j = E_i^j / E^j$  is the energy probability of the  $i$ th component of  $D^j$ ,  $E^j$  is the total

energy of the coefficients in band  $j$  as calculated by  $[E_j = \sum_i (D_j^i)^2 \quad j = 1, 2, \dots n]$ ,

and  $E_i^j = |D_i^j|^2$ . The energy entropy measures the magnitude of signal fluctuations.

(3) Ultimate width. For any signal  $X = \{x_1, x_2, \dots, x_N\}$ , the ultimate width is defined as  $\text{width} = \frac{2\sigma}{\mu}$  where  $\mu$  and  $\sigma$  are the mean and variance of signal  $X$ . A large width indicates sharp variations.

### 3.2 Geometric based irregularity measures

At each significant level  $j$ , a supposed structural component  $C_j$ ,  $s \geq j \geq s_t$  of a contour is reconstructed from the wavelet coefficients,  $C_j = A^s + D^s + \dots + D^j$ . In addition to a simple variance measure (4), the other irregularity measures of the reconstructed contours are evaluated as:

$$(5) \text{ Radial Deviation, } RD = \frac{1}{N} \sum_{i=1}^N |(r_i - \bar{r})|$$

where  $\bar{r}$  is the mean radius of the contour signature.

$$(6) \text{ Contour Roughness, } R_o = \frac{1}{N} \sum_{i=1}^N |r_i - r_{i+1}|$$

$$(7) \text{ Irregularity Measure, } IM = \frac{\text{Area}(C_j \oplus S_s)}{\text{Area}(S_s)}$$

where  $S_s$  is reconstructed from the approximate data,  $A^s$ , at the significant level  $s$ , and  $\oplus$  is the exclusive-or operator.

With the seven irregularity measures described above and the four significant sub-bands ( $D^6$ ,  $D^7$ ,  $D^8$ , and  $D^9$ ), there would be a total of 25 features: measures (1) to (6) for each of the four significant sub-bands (24 features thus far), and  $IM$  (irregularity measure 7) at the threshold scale  $s_t$ . However, these features were filtered to remove redundancy. This was done by a correlation analysis followed by performance based feature selection. Correlation analysis computes the correlation coefficient for a pair of features  $t_i$ ,  $t_j$ , from a feature vector  $F = \{t_1, t_2, \dots, t_n\}$  and a sample set  $S = \{x_1, x_2, \dots, x_m\}$ . A large correlation coefficient indicates redundancy [17]. The performance based feature selection requires calculating the probability distribution of each feature's contribution to a correct classification, tested on both benign and malignant sample sets. The accumulated probability is found, then each feature is verified with an established classification error threshold [17].

Once the correlation analysis and the performance based feature selection was executed, 12 of the original 25 features were removed due to redundancy. The remaining 13 features are Average Energy(1) for sub-band 6-8; Wavelet Entropy(2) for sub-bands 6-9; Ultimate Width(3) for sub-bands 6, 7 and 9; Radial Deviation(5) for sub-band 6; Contour Roughness(6) for sub-band 7; and Irregularity Measure(7) for sub-band 6. The selected and eliminated features are displayed in Table 3.

Table 3 - Final feature selection

| Sub-band | Average energy | Wavelet Entropy | Ultimate Width | Variance | Radial deviation | Contour roughness | Irregularity measure |
|----------|----------------|-----------------|----------------|----------|------------------|-------------------|----------------------|
| 6        | ✓              | ✓               | ✓              |          | ✓                |                   | ✓                    |
| 7        | ✓              | ✓               | ✓              |          | ✓                |                   |                      |
| 8        | ✓              | ✓               |                |          |                  |                   |                      |
| 9        |                | ✓               | ✓              |          |                  |                   |                      |

Table in accordance to information from MA, L.; STAUNTON, R.C. [17]

Similarly to the significant sub-band selection procedure, as the redundant features were previously identified during Ma and Staunton's study, with the approval of Li Ma, the identification of redundant features was not done; the re-implementation uses the final feature selection directly.

## 5. IMPLEMENTATION

This chapter details the development of the algorithms for the three additional metrics used in this experiment. Difficulties encountered and modifications to the original plan of action are included due to their contribution to the overall knowledge acquired and possibly influence over final results. First the edge detector used is described due to its fundamental contribution to the outcome of the algorithm, followed by the implementation of algorithms for the simple geometric border irregularity metric the asymmetry metric and color change metric. A proposed algorithm for computing diameter size is also presented.

### 5.1 Canny Edge Detector

In order to perform the calculations for each metric in the ABCD criteria, it is necessary to first single out the skin lesion from the image, obtaining a sequence of coordinates of its contour. There are many edge detection algorithms that could be used, the one selected for this study is the Canny Edge Detector, developed by John Canny. The algorithm, detailed in the monograph *A Computational Approach to Edge Detection* [3], is notably effective and as such it is ubiquitously used. A comparison with the Laplacian of Gaussian, Robert, Prewitt, and Sobel edge detector operators has shown that in almost all scenarios, the Canny Edge Detector exhibited superior performance, albeit with the disadvantage of being computationally more expensive [18]. However, as the amount of data to be processed is not inordinate, computational time may be sacrificed to gain accuracy in edge detection. Additionally, the hysteresis thresholding component of the Canny Edge Detector allows a form of customization to a specific detection objective, as is the case with extracting the contour of the skin lesion.

The Canny Edge Detector algorithm can be resumed in four main steps: Image filtering; gradient magnitude computing; Non-maximum suppression and hysteresis thresholding to trace the edges.

## 1 - Image filtering

The Canny Edge detector is highly susceptible to noise; the first step in the algorithm is filtering the image to reduce the misleading effect of noise pixels through a step edge detector. Canny calculated the optimal filter for this task, named ‘Filter number 6’ in his article [3]. However, he observed that although the first derivative of Gaussian operator performed approximately 20% worse than the optimal operator in the performance evaluations, this difference is hardly noticeable when visualizing their effects on real images. Figure 8 contains a graph showing the similarities between the optimal step edge operator and the first derivative of a Gaussian. As the optimal operator requires much more computational effort than the first derivative of the Gaussian, the image is convolved with a Gaussian filter to obtain the desired noise reduction.

Figure 8 - Comparison of optimal and Gaussian operator.

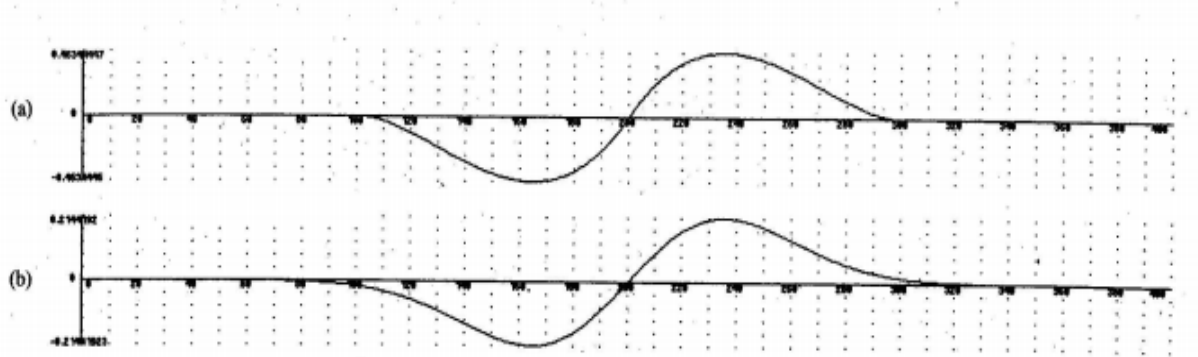


Fig. 6. (a) The optimal step edge operator. (b) The first derivative of a Gaussian.

Source: CANNY, John. [3]

## 2 - Gradient magnitude computing

The gradient of an image indicates the direction of a rapid change in intensity and as such provides information regarding the orientation of the edge, whether it is horizontal, vertical or diagonal. In a two dimensional coordinate system as is this case, the gradient is given by

$$\nabla f = \frac{\partial f}{\partial x} + \frac{\partial f}{\partial y}$$

the vector composed of the partial derivatives of  $f$ . A horizontal gradient is given by

$$\nabla f = 0 + \frac{\partial f}{\partial y}$$

as the change is in the  $y$  direction; a vertical gradient is given by

$$\nabla f = \frac{\partial f}{\partial x} + 0$$

as the change is in the  $x$  direction. The magnitude of the gradient is given by

$$\|\nabla f\| = \sqrt{\left(\frac{\partial f}{\partial x}\right)^2 + \left(\frac{\partial f}{\partial y}\right)^2}$$

and is calculated for every pixel in the image.

### 3 - Non-maximum suppression

Once the gradient magnitude calculation is performed on each pixel, its value is then verified to determine whether it assumes a local maximum in the gradient direction. The gradient direction is given by

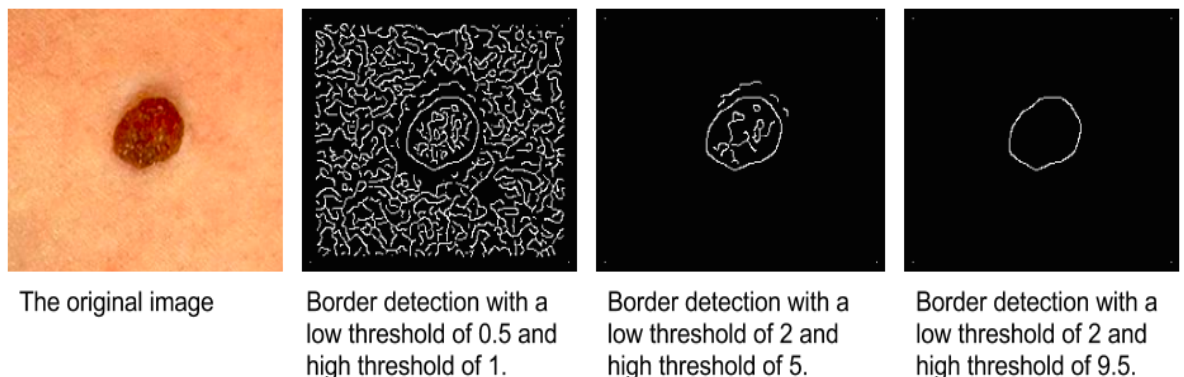
$$\theta = \tan^{-1} \left( \frac{\frac{\partial f}{\partial x}}{\frac{\partial f}{\partial y}} \right)$$

The implementation of the algorithm does not compute the gradient direction so as to avoid performing a division calculation. Instead, the two derivatives are checked for the same sign and then the largest of the two derivatives is singled out. The pixel magnitude is then compared to its two neighbor's values in the four possible directions, these being north - south, east - west, northeast - southwest and northwest-southeast. Linear interpolation is used between the two neighbor pixels for greater accuracy. Only local maximums are considered edge candidates, therefore if the central pixel's magnitude is not greater than that of its two neighbors it is suppressed' by setting its edge strength value to zero.

### 4 - Hysteresis thresholding

The pixels that correspond to a local maximum and in effect possess a high edge strength value are set aside as the edges detected in the image. Yet the selected edge pixels can be further refined through specifying a threshold as the final comparison to determine an existing edge. Hysteresis thresholding is done using a low and a high threshold. The low threshold detects weak edges and the high threshold the strong edges. It was necessary to experiment to determine the optimal combination of thresholds for the situation in question, that of singling out the skin lesion in the image. The effects of different threshold levels can be seen in Figure 9.

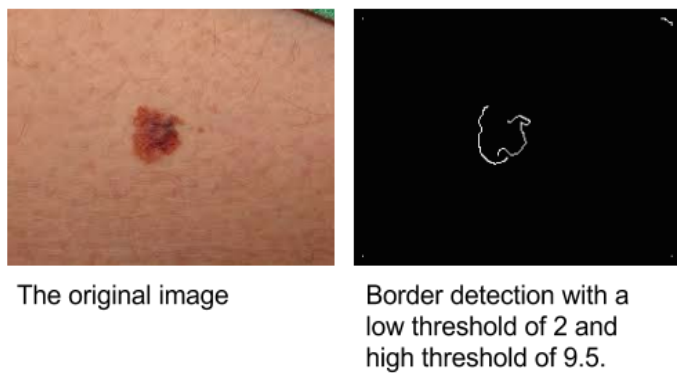
Figure 9 - Threshold performance comparison



Source: Testing performed on March 2nd, 2014.

The low threshold detected texture traces and fine edges; as the skin lesion has a considerably distinct edge a high threshold was proven to be the most adequate. With melanoma lesions the contour is not continuous (See Figure 10); this of course is expected due to the lesion's characteristic asymmetry, border irregularity and color change. Ergo, it is presumed that this will not be misleading in the final results.

Figure 10 - Threshold performance on image of melanoma



Source: Testing performed on March 2nd, 2014.

During the course of testing, it became apparent that the algorithm as it is will only function properly if applied to images with a single lesion. Additionally, the images may need to be adapted to eliminate non-skin elements. In Figure 5, the original image shows what appears to be the hem of an item of clothing in the upper right corner. This is classified as a strong border as displayed in the image tracing the detected borders; if not treated, it will be inaccurately handled as part of the skin lesion in the subsequent

phases of the algorithm.

The re-implementation of Ma and Staunton's algorithm was written in Octave, which has a built-in Canny Edge Detector function. The geometric Border Irregularity Asymmetry and Color change metric algorithms were written in Java. For this phase of the process, Tom Gibara's Java implementation of the Canny Edge Detector [8] algorithm is used. The implementation of the Canny Border Detector developed by Tom Gibara was slightly modified so as to return a list of coordinates of the detected edge pixels as opposed to an image of the traced edges.

## **5.2 AB\*CD Metrics**

### **5.2.1 Asymmetry metric**

Asymmetrical skin growths, in which one part is different from the other, may indicate melanoma. [30]

Symmetry is defined mathematically as invariability regardless of transformations, an absolute characteristic that cannot be measured in degrees [10]. Due to this most rigid definition, rarely if ever is it possible to label a naturally formed figure as symmetrical [10]. As the images to be analyzed are of the human body, it is safe to assume that all the figures will be asymmetric. As symmetry cannot be measured, the symmetry metric used in this algorithm is the number of rotational symmetries identified with a 10% tolerance for imperfection. As such, the symmetries detected and numbered will not be perfectly symmetrical.

In examining skin blemishes, rotation and reflection symmetry is of greater relevance. Two of the more recent rotation/reflection symmetry detection algorithms are Loy and Eklundh's Detecting symmetry and symmetric constellations of features [16] and Prasad and Davis' Detection rotational symmetries [26]. Loy and Eklundh's algorithm is feature based; it uses pairwise matching and voting for symmetry foci in a Hough transform to identify asymmetry. Prasad and Davis created an algorithm that filters in an input color image into a gradient vector flow field, extracting and matching the features into the gradient vector flow field, using a voting scheme for symmetry detection.

A comparative analysis of both algorithms [4] shows that the first algorithm has a higher sensitivity rate than the second; however it also presents very high false-positive rates which are of serious consequence in the medical field.

Tom Gibara's Symmetry Detection Algorithm [9] provides a method to measure asymmetry using a comparative threshold to identify rotational symmetries, more easily applicable to the analysis of the skin blemishes.

The algorithm proceeds as follows:

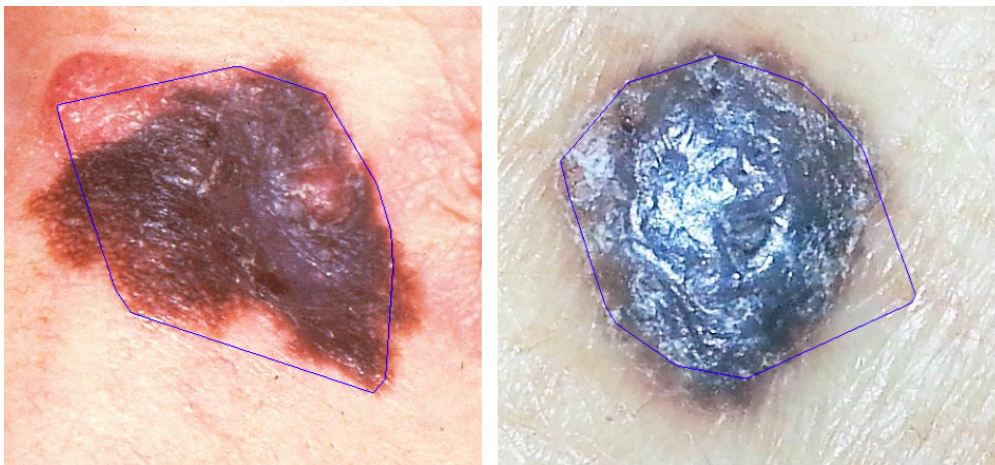
1. Identify the centroid of the object.
2. Measure the object radius (distance from centroid to most distant object pixel).
3. Choose a set of circles centered on the centroid with radius less than the object radius.
4. Sample the image at a fixed angular resolution (an even number of equiangular points) to create a vector of pixel values for each circle.
5. 'Convolve' each vector with itself to create a new set of vectors. These loosely measure the reflectional symmetry across the angle associated with each element.
6. Sum all of the resulting vectors to obtain an overall symmetry score for each angle considered.
7. Disregard any angle that does not exceed a predetermined threshold and which is not a local maximum.
8. Of the remaining angles, calculate the score-weighted average of adjacent angles (subject to a predefined threshold).
9. The resulting angles, together with the centroid, define a set of axes along which reflectional symmetry is high.

Source: GIBARA, TOM. [9]

Before running the Symmetry Detector on the images, it is necessary to delimit the region to be examined. The border traced by the Canny Edge Detector will likely not provide a continuous contour for images of melanoma lesions as they are generally multi-colored and without distinct borders (See *Figure 5*). As it happens, there is no guarantee that even the analysis of benign lesions will result in a continuous contour.

The solution to this issue is found in Yuri Pourre's implementation of the Quick Hull algorithm [25], which draws the smallest polygon possible given a set of coordinates. Once the Canny Edge Detector is run on the image, the resulting list of coordinates of the detected edge pixels is fed into the Quick Hull program.

Figure 11 - Polygon containing the skin lesion: Melanoma and Neoplasm

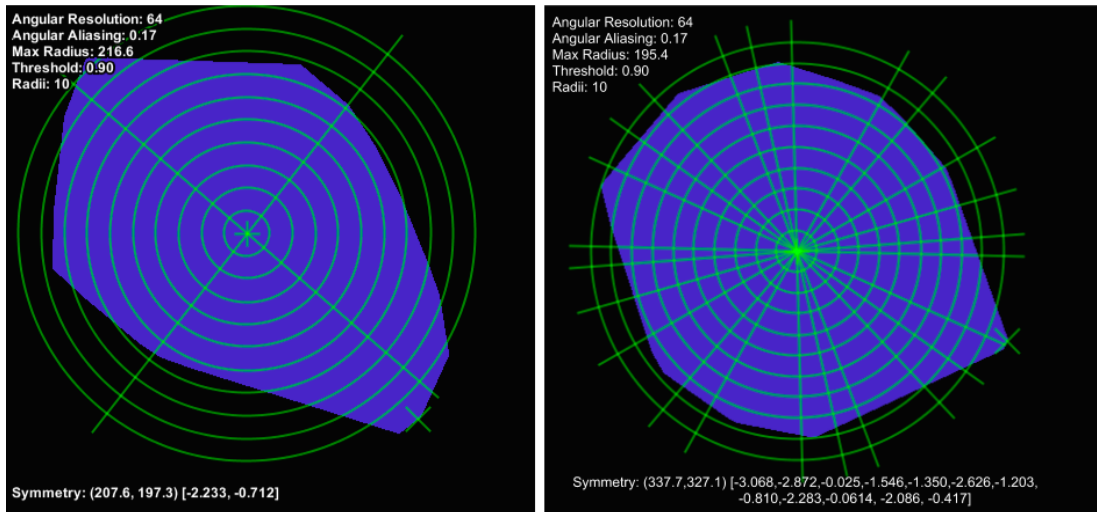


Source: Testing performed on March 9th, 2014.

An image with the polygon outline is then filled in and converted to grayscale for compatibility with Gibara's Symmetry Detector algorithm. The important algorithm parameters [9] are Angular Resolution, Angular Aliasing, Radius Count ('Radii' in the sample output in Figure 8), and Threshold. The Angular Resolution is the number of sample arcs in the circle. Angular Aliasing is the smallest angle permitted between identified axes of symmetry. Angles closer together than this value are combined into a single angle. Radii indicates the number of different radii at which samples are taken. Threshold is the proportion of the maximum possible score that an angle must obtain to be considered. Once the detector is run, a summary of the execution is displayed. The above parameters and their respective values are listed. Blue pixels indicate pixels identified with the object, in this case the polygon surrounding the skin lesion. The green 'plus' indicates the position of the centroid, currently not visible due to the many traced lines of reflectional symmetry. The green 'cross' indicates a pixel at maximum distance from the centroid. Green circles indicate the circles from which samples of image data were taken. Green lines indicate the lines of reflectional symmetry identified by the algorithm. The array of numbers in between the square brackets indicate the

location of the symmetries identified. The size of this array is the amount of symmetries identified.

Figure 12 - Summary of Symmetry Detector results: Melanoma and Neoplasm



Source: Testing performed on March 9th, 2014.

### 5.2.2 B - Border Irregularity metric

Melanomas may have borders that are vaguely defined. Growths with irregular, notched or scalloped borders need to be examined by a doctor [30].

Staunton and Ma's analysis of border irregularity used both statistical and geometrical measures of the structural component of the skin lesion. To observe the added value of removing the textural component from the calculation and the utilization of statistical measures in addition to geometrical, a simple geometric border irregularity metric was developed. Succinctly, it is the coefficient of variance of the lesion's radii. This was done in Staunton and Ma's algorithm, however the calculation was performed on the extracted structural component; in this metric all edges detected from the lesion are used, both structural and textural. The algorithm to obtain the simple border irregularity metric is detailed below:

1. A list of coordinates of the lesion's border is obtained from the Canny Edge Detector;
2. The centroid of the lesion would calculated by finding the mean  $x$  and  $y$  values;

however as the contour of melanoma lesions is not continuous, it was necessary to correct this formula. The coordinates of the centroid are the minimum value  $x$  and  $y$  plus an offset of the difference between the maximum and minimum value of  $x$  and  $y$  divided by 2.

$$C_x = x_m + (x_M - x_m)/2 \quad C_y = y_m + (y_M - y_m)/2$$

3. The mean radius is obtained by calculating the average of the euclidean distance between the centroid and each point in the list of border coordinates;
4. The standard deviation is given by

$$\sigma = \sqrt{\frac{1}{n} \sum_{i=1}^n (r_i - \bar{r})^2}$$

with  $n$  as the number of coordinate pairs (points) in the list,  $r_i$  as the radius at point  $i$  and  $\bar{r}$  as the mean radius. Bias correction is unnecessary given the sample is equal to the population.

5. Obtain the coefficient of variance given by

$$c_v = \frac{\sigma}{\mu}$$

being that  $\mu$  is the mean radius calculated in step 3.

An example of the calculated metric is displayed in Figure 13, for both a benign neoplasm and melanoma.

Figure 13 - Comparison of simple border irregularity metric



Image of a benign growth and the tracing in white of the detected edge and centroid.  
Border Irregularity metric: 0.107

Image of a melanoma lesion and the tracing in white of the detected edge and centroid.  
Border Irregularity metric: 0.132

Source: Testing performed on March 5th, 2014.

### 5.2.3 C - Color Changes

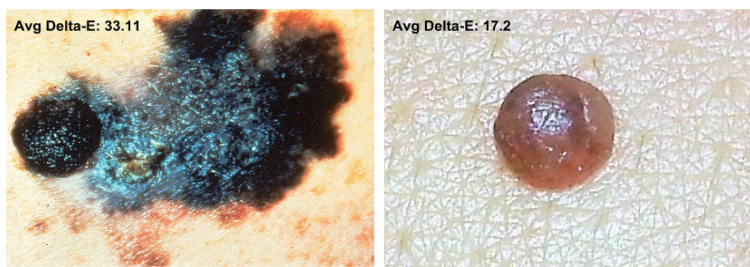
Multiple colors or uneven distribution of color may indicate cancer. [30]

Depending on the resolution and lighting of the image taken of the skin lesion, color variance may be noticeable even in benign lesions. This makes it necessary once again to measure the difference between colors in the lesion and compare this difference to a defined threshold. The difference between colors is represented by Delta-E, a metric established by the International Commission on Illumination (CIE) to quantify color differences [31]. The first Delta-E formula was developed in 1976; since then more sophisticated formulae have been developed and approved by CIE [31]. As the subsequent Delta-E versions are of a more complex nature and consequentially more computationally expensive, the 1976 CIELAB is used in this study. A suggestion of ongoing work is to experiment using the other Delta-E formulae to determine whether there is significant increase in efficiency in analyzing the color variegation of skin lesions. Using the CIELAB, the algorithm is quite straightforward:

1. Identify lesion borders within the image using the Canny edge detector;
2. Delimit a region to analyze color change including all detected edges;
3. Calculate the average color of the lesion;
4. Convert the average color of the lesion from RGB to L\*a\*b\*;
5. Iterate through each pixel in the delimited region;
  - 5.1 Convert the color of the pixel from RGB to L\*a\*b\*;
  - 5.2 Calculate the CIELAB Delta-E of the pixel color and average color;
6. Return the average Delta-E of the region.

Yuri Pourre's implementation of the Quick Hull algorithm was used. In addition to this, Pourre contributed with a function to determine the average color of a given region. In sum, the color change metric is the average Delta-E of each pixel in the lesion compared to the average color of the lesion.

Figure 14 - Comparison of Melanoma and Neoplasm Average Delta-E



Source: Testing performed on May 2nd, 2014.

#### **5.2.4 D - Diameter greater than 6mm**

A skin growth's large size may be an indication of cancer. [30]

The schedule limitations of this project difficulted the development of an algorithm to measure the lesion diameter. As there is potential in exploring the use of lesion diameter in image analysis, a suggested method is described to obtain this metric.

This final criteria presents a challenge for the application of computerized image analysis; the images will be taken at different ranges with no comparative figure, impairing an accurate calculation of real size. A proposed solution is to identify the pores in the image and measure the average distance between them in pixels; this would provide a scale of the lesion's diameter. An adaptation of Q. Zhang and T. Whangbo's Skin Pores Detection Algorithm [29] could be implemented to find the pores in the image and note their coordinates so as to determine the distance between them. The algorithm is based on image segmentation. A preprocessing algorithm to balance the illumination of the image must be run before the pore detection algorithm. The Global Luminance Proportion algorithm is noted below.

Using the original image of MxN size:

1. a. Calculate the average luminance of the image;
- b. Split the image S into V sub-blocks, calculating the average luminance;
- c. Obtain luminance difference matrix D;
2. Interpolation algorithm for matrix D until element number in matrix equals MxN;
3. Merge matrix D and original image S into new image sized MxN.

When the image has balanced luminance, the segmentation is performed using the Fuzzy C-Means Algorithm. After this segmentation, pixels in the image are labeled to 8 connectivity and skin pores can be classified from the 8-connectivity labeled image by calculating the quadratic moment and the ration between row and column moments.

## 6. ANALYSIS

### 6.1 Pre-Processing

To reduce the amount of data to be processed and expedite the algorithms' execution, the images were cropped to the minimum size while still containing the lesion in its entirety. This was performed manually.

During the delimitation of the lesion within the image using the Canny Edge Detector, it was observed that a single set of low and high thresholds was not enough to cater to all the images in the database. When an image was slightly blurred or when the lesion, regardless of being malignant or benign, presented similar color to the surrounding skin, the Canny Edge Detector failed to identify edges in the image. Lowering the threshold was not an option as that added noise and detected skin texture in other images. To solve this problem, two sets of thresholds were used: a standard set of [6, 13] for the low and high threshold respectively, and a second set of [2, 8] for images that failed to return more than 70 edge coordinates. Of the 70 images analyzed, 12 utilized the second set of thresholds. These thresholds were established after successive tests and manual examinations of the results; there is no evidence that they are the optimal selection.

### 6.2 Dataset

The images used in training and testing the classifier were obtained from the Dermatlas Interactive Dermatology Atlas and the records of Dr. Jefferson B. Louback and Dr. Ricardo Barbosa, a total of 70 images. A total of 32 of the images are of malignant melanomas and 38 are of various types of benign neoplasms. The images from Dermatlas are from various sources, among them both organizations and medical professionals. To provide a reference to the image's source, each image ID (file name) contains a specific prefix: RB for Ricardo Barbosa M.D.; JL for Jefferson Louback M.D.; AC for Armand Cognetta, M.D.; RU for Richard Usatine, M.D.; SCF for Skin Cancer Foundation; SS for Skin Surgery: A Practical Guide.

The images from Dermatlas had a numerical ID; this number is maintained in the dataset. Dr. Barbosa and Dr. Louback's records also were numbered and these

numbers were also maintained. Images of malignant lesions is marked with an ‘M’ and images of benign lesions with an ‘N’. An example of the ID of an image of a malignant lesion from Dr. Barbosa’s records is “M142\_RB”: M for malignant, 142 is the numbering provided by Dr. Barbosa’s records, RB is his initials. All of the images used were submitted for diagnosis confirmation to Dr. Louback.

There is a total of 17 features in the algorithms used, these being Staunton and Ma’s 14 features and the 3 additional ones for Asymmetry, Border Irregularity and Color change. However, the implementation for the Irregularity Measure based on the approximate data, one of Staunton and Ma’s features, was not validated and was not included in the final analysis.

### 6.3 Data Analysis

To perform the classification, the Waikato Environment for Knowledge Analysis (Weka<sup>1</sup>) software was used. Developed at the university of Waikato, it contains a collection of machine learning algorithms written in Java and is licensed under the GNU General Public License.

To separate the test and training data, a percentage split of 28% was done to emulate the optimum size of the training set determined by Staunton and Ma, which is 18 instances (half malignant, half benign) [17]. In Staunton and Ma’s study, a Back Projection neural network was used as the training algorithm. However, as occasionally some features returned undefined values, a Naïve Bayes classifier was also used due to its ability in dealing with missing data [20].

The Multilayer Perceptron (Weka’s neural net with Back Propagation) presented better performance than the Naïve Bayes classifier, as seen in Table 4.

Table 4 - BP Neural Net and Naïve Bayes performance

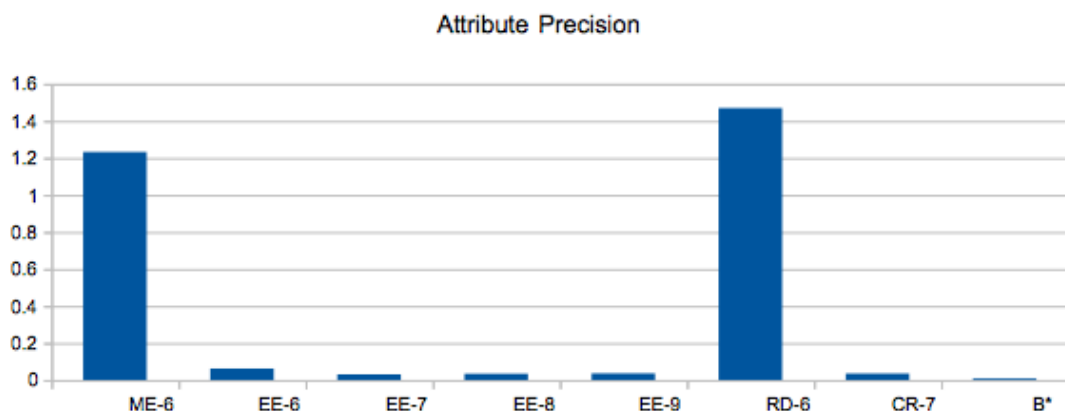
| <b>==== BP Neural Net ====</b>              |         |           |          |       |  | <b>==== Naïve Bayes ====</b>                |         |           |          |       |  |
|---|---------|-----------|----------|-------|--|---|---------|-----------|----------|-------|--|
|   |         |           |          |       |  |   |         |           |          |       |  |
| Correctly Classified Instances              |         |           |          |       |  | 73.6842 %                                   |         |           |          |       |  |
| Incorrectly Classified Instances            |         |           |          |       |  | 26.3158 %                                   |         |           |          |       |  |
| <b>==== Detailed Accuracy By Class ====</b> |         |           |          |       |  | <b>==== Detailed Accuracy By Class ====</b> |         |           |          |       |  |
| TP Rate                                     | FP Rate | Precision | ROC Area | Class |  | TP Rate                                     | FP Rate | Precision | ROC Area | Class |  |
| 0.778                                       | 0.3     | 0.7       | 0.747    | true  |  | 0.556                                       | 0.125   | 0.833     | 0.639    | true  |  |
| 0.7   | .222    | 0778      | 0.747    | false |  | 0.875                                       | 0.444   | 0.636     | 0.639    | false |  |

Source: <sup>1</sup>Weka classifier output

<sup>1</sup> <http://www.cs.waikato.ac.nz/ml/weka/>

When including the simple Border Irregularity Metric (See section 4.3.2) in the analysis, the accuracy was not altered, both in the BP Neural Net model and the Naïve Bayes. Figure 15 compares the added precision of the simple Border Irregularity Metric (which for the remainder of the monograph is referred to as  $B^*$ ) and the 7 attributes with the least precision of Staunton and Ma's 13 features using a Naïve Bayes model (The remaining 6 presented extremely high levels of precision and could not be compared in the same graph). Table 5 shows the relation between the features and the abbreviations used in the graphs and dataset.

Figure 15 - Comparison of  $B^*$  metric precision



Source: Based on data from the Weka classifier

Table 5 - Abbreviation glossary

|       |                                   |
|-------|-----------------------------------|
| ME-6  | Mean Energy of sub-band 6         |
| ME-7  | Mean Energy of sub-band 7         |
| ME-8  | Mean Energy of sub-band 8         |
| EE-6  | Energy Entropy of sub-band 6      |
| EE-7  | Energy Entropy of sub-band 7      |
| EE-8  | Energy Entropy of sub-band 8      |
| EE-9  | Energy Entropy of sub-band 9      |
| UW-6  | Ultimate Width of sub-band 6      |
| UW-7  | Ultimate Width of sub-band 7      |
| UW-9  | Ultimate Width of sub-band 9      |
| RD-6  | Radial Deviation of sub-band 6    |
| CR-7  | Contour Roughness of sub-band 7   |
| A     | Asymmetry metric                  |
| $B^*$ | Simple Border Irregularity metric |
| C     | Color change metric               |

A second round of analysis was performed, this time including the Asymmetry and Color Change metric. This addition increased the performance of both the BP neural net and Naïve Bayes model. The specifics of each classification are listed in Table 6 and Table 7.

Table 6 - Comparison: StauntonMa + A + C with BP Neural Net

| <b>StauntonMa</b>                           |                | <b>StauntonMa + A + C</b>        |                 |
|---|----------------|----------------------------------|-----------------|
| <b>==== BP Neural Net ====</b>              |                | <b>==== BP Neural Net ====</b>   |                 |
| Correctly Classified Instances              | 73.6842 %      | Correctly Classified Instances   | 76.3158 %       |
| Incorrectly Classified Instances            | 26.3158 %      | Incorrectly Classified Instances | 23.684 %        |
| <b>==== Detailed Accuracy By Class ====</b> |                |                                  |                 |
| <b>TP Rate</b>                              | <b>FP Rate</b> | <b>Precision</b>                 | <b>ROC Area</b> |
| 0.778                                       | 0.3            | 0.7                              | 0.747 true      |
| 0.7   | 0.222          | 0.778                            | 0.747 false     |
| <b>TP Rate</b>                              |                | <b>TP Rate</b>                   |                 |
| 0.833                                       |                | 0.833                            |                 |
| 0.7   |                | 0.167                            |                 |
| <b>FP Rate</b>                              |                | <b>FP Rate</b>                   |                 |
| 0.3   |                | 0.3                              |                 |
| <b>Precision</b>                            |                | <b>Precision</b>                 |                 |
| 0.714                                       |                | 0.714                            |                 |
| <b>ROC Area</b>                             |                | <b>ROC Area</b>                  |                 |
| 0.803                                       |                | 0.803                            |                 |
| true  |                | false                            |                 |

Source: Excerpts of Weka classifier output

Table 7 - Comparison: StauntonMa + A + C with Naïve Bayes

| <b>StauntonMA</b>                           |                | <b>StauntonMa +A +C</b>          |                 |
|---|----------------|----------------------------------|-----------------|
| <b>==== Naïve Bayes ====</b>                |                | <b>==== Naïve Bayes ====</b>     |                 |
| Correctly Classified Instances              | 70.5882 %      | Correctly Classified Instances   | 76.4706 %       |
| Incorrectly Classified Instances            | 29.4118 %      | Incorrectly Classified Instances | 23.5294 %       |
| <b>==== Detailed Accuracy By Class ====</b> |                |                                  |                 |
| <b>TP Rate</b>                              | <b>FP Rate</b> | <b>Precision</b>                 | <b>ROC Area</b> |
| 0.556                                       | 0.125          | 0.833                            | 0.639 true      |
| 0.875                                       | 0.444          | 0.636                            | 0.639 false     |
| <b>TP Rate</b>                              |                | <b>TP Rate</b>                   |                 |
| 0.667                                       |                | 0.667                            |                 |
| 0.125                                       |                | 0.125                            |                 |
| <b>FP Rate</b>                              |                | <b>FP Rate</b>                   |                 |
| 0.857                                       |                | 0.857                            |                 |
| <b>Precision</b>                            |                | <b>Precision</b>                 |                 |
| 0.806                                       |                | 0.806                            |                 |
| true  |                | false                            |                 |
| <b>ROC Area</b>                             |                | <b>ROC Area</b>                  |                 |
| 0.806                                       |                | 0.806                            |                 |
| false                                       |                | true                             |                 |

Source: Excerpts of Weka classifier output

## 7. CONCLUSION

A significant disclaimer to the findings of this experiment is that none of the images of skin lesion in the dataset were of darkly pigmented skin. It has not been determined whether this would affect the outcome of the algorithm. Additionally, there are abnormalities in both benign neoplasms and malignant melanomas that are likely to be misleading. According to Dr. Jefferson B. Louback, the Amelanotic Melanoma variety can be the same color as the surrounding skin, and as such would possibility not be detected by the algorithm. The Congenital Melanocytic Nevus, in layman's terms, a birthmark, often doesn't adhere to the typical benign neoplasm traits. Samples of these specific variations were also not in the dataset, although a series of atypical nevi (benign neoplasms) were included. In sum, digital image analysis can be an effective identifier of a wide range of melanomas and may contribute to an early diagnosis. However, it remains necessary to obtain a medical confirmation.

Based on the analysis performed, it is safe to conclude that in measuring lesion border irregularity to diagnose melanoma it is essential to extract the structural components, as proposed by Staunton and Ma [17]. As seen in Table 4, a geometric border irregularity measure based on raw data containing both structural and textural components did not add accuracy due to insignificant precision. It is curious to observe in Figure 15 how the  $B^*$  metric fared in comparison to RD-6 and CR-7;  $B^*$  being the geometric irregularity measure of raw data with precision of 0.008 and RD-6 and CR-7 being geometric irregularity measures of only structural data with precision of 1.46 and 0.035.

Although the performance of Staunton and Ma's algorithm is certainly noteworthy, it was observed that the inclusion of metrics for asymmetry and color change added substantial precision. In Tables 6 and 7 we see the accuracy leap from from 73.68% to 76.31% when using a BP neural net, and from 70.58% to 76.47% using Naïve Bayes. There was also an increase in the area under the ROC curve of 7.5% and 25% respectively. It is therefore suggested that algorithms to diagnose melanoma by studying digital images of skin lesions only stand to gain by using metrics for Asymmetry, Border Irregularity, and Color Change in conjunction.

## References

- [1] ABASSI, Naheed R. et al. Early Diagnosis of Cutaneous Melanoma: Revisiting the ABCD Criteria. **Journal of the American Medical Association**, December 8, 2004, Vol 292, No. 22
- [2] ANEJA, S; ANEJA, S; BORDEAUX J.S. **Association of Increased Dermatologic Density With Lower Melanoma Mortality**. Case Western Reserve University, Yale University School of Medicine, 2012.
- [3] CANNY, John. **A Computational Approach to Edge Detection**. IEE Transactions on Pattern Analysis and Machine Intelligence, Vol. PAMI-8, NO. 6, November 1986.
- [4] CHEN, Po-chen et. al. **A Quantitative Evaluation of Symmetry Detection Algorithms**. 17 pages. Penn State University & Carnegie Mellon University, 2007.
- [5] CLAWSON, K.M. et al. **Analysis of Pigmented Skin Lesion Border Irregularity Using the Harmonic Wavelet Transform**. Machine Vision and Image Processing Conference, 2009. IMVIP '09.
- [6] DAUBECHIES, Ingrid. **Where do wavelets come from? - A personal point of view**. Department of Mathematics and Program in Applied and Computational Mathematics, Princeton University.
- [7] FRIEDMAN, R. J.; RIGEL, D. S.; KOPF, A. W. Early Detection of Malignant Melanoma: The Role of Physician Examination and Self-Examination of the Skin. **CA Cancer Journal for Clinicians**. 1985 May-Jun;35(3):130-51
- [8] GIBARA, Tom. **Canny Edge Detector Implementation**. Available at: <<http://www.tomgibara.com/>>. Accessed on January 23rd, 2014.
- [9] GIBARA, Tom. **Symmetry Detection algorithm**. Available at: <<http://www.tomgibara.com/>>. Accessed on January 23rd, 2014.
- [10] GLERUP, Nanna. **Asymmetry measures in medical image analysis**. 174 pages. Department of Innovation, IT University of Copenhagen, 2005.
- [11] JING, Li et al., Brief Introduction of Back Propagation (BP) Neural Network Algorithm and Its Improvement. **Advances in Intelligent and Soft Computing** Volume 169, 2012, pp 553-558

- [12] JORGENSEN, P.E.T.; SONG, M.-S. **Comparison of Discrete and Continuous Wavelet Transforms**. Springer Encyclopedia of Complexity and Systems Science, Springer, 2008.
- [13] KIMBALL, A.B.; RESNECK, J.S. The US dermatology workforce: a specialty remains in shortage. *Journal of the American Academy of Dermatology*, 2008 Nov; 59(5):741-5.
- [14] KURUGANTI, P.T.; HAIRONG, Qi. **Asymmetry analysis in breast cancer detection using thermal infrared images**. Engineering in Medicine and Biology, 2002. 24th Annual Conference and the Annual Fall Meeting of the Biomedical Engineering Society EMBS/BMES Conference, 2002. Proceedings of the Second Joint.
- [15] LEE, Tim K. et al. **Irregularity index: A new border irregularity measure for cutaneous melanocytic lesions**. Vancouver: Elsevier, 2003.
- [16] LOY, G.; EKLUNDH, J. **Detecting symmetry and symmetric constellations of features**. European Conference on Computer Vision (ECCV'04), Part II, LNCS 3952, pages 508,521, 2006.
- [17] MA, L.; STAUNTON, R.C. **Analysis of the contour structural irregularity of skin lesions using wavelet decomposition**. Hangzhou Dianzi University & University of Warwick, 2012.
- [18] MAINI, R.; AGGARWAL, H. Study and Comparison of Various Image Edge Detection Techniques. **International Journal of Image Processing (IJIP)**, Volume (3) : Issue (1)
- [19] McKOY, Karen. **The Importance of Dermatology in Global Health**. Harvard Medical School Department of Dermatology.
- [20] MERETAKIS, Dimitris; WÜTHRICH, Beat. **Extending naïve Bayes classifiers using long itemsets**. Proceedings of the fifth ACM SIGKDD international conference on Knowledge discovery and data mining, Pages 165-174. 1999
- [21] MONTEIRO, Fábio. Saúde privada não consegue administrar o aumento da procura. **Correio Braziliense**, May 2011.
- [22] MORLET, J. et al. Wave propagation and sampling theory. **Geophysics**, VOL. 47, NO. 2, Pages 203-221, February 1982.
- [23] NACHBAR, Franz et al. The ABCD rule of dermatoscopy. **Journal of the American Academy of Dermatology**, Volume 30, Issue 4 , Pages 551-559, April 1994.

- [24] NEWLAND, David E. **Harmonic Wavelet Analysis**. Department of Engineering, University of Cambridge, 1993.
- [25] POURRE, Yuri. **Quick Hull Algorithm**. Available at: <<https://github.com/yuripourre/>>. Accessed on March 5th, 2014.
- [26] PRASAD, V.;DAVIS, L. **Detection rotational symmetries**. IEEE International Conference on Computer Vision (ICCV), pages 346–352, 2005.
- [27] RICOTTI, Charles et al., Malignant Skin Neoplasms. **Medical Clinics of North America**, Vol. 93, Issue 6, Pages 1241-1264
- [28] THOMAS, L. et al., **Semiological Value of ABCDE Criteria in the Diagnosis of Cutaneous Pigmented Tumors**. Unité de Dermatologie et Département d’Informatique Médicale des Hospices Civils de Lyon, Hôpital de l’Hôtel-Dieu, Lyon, France Dermatology, 1998.
- [29] ZHANG, Qian; WHANGBO, Taeg Keun. **Skin Pores Detection for Image-Based Skin Analysis**. 5 pages. Department of Computer Science, Kyungwon University, 2008.
- [30] **Melanoma pictures to help identify skin cancer**. Available at: <<http://www.mayoclinic.com/health/melanoma/DS00575>>. Accessed on October 19th 2013.
- [31] **Joint ISO/CIE standard**.CIE Colorimetry - Part 4: 1976 L\*a\*b\* Colour Space.ISO 11664-4:2008(E)/CIE S 014-4/E:2007

## **Appendix I - Dataset**

| ID            | ME-6   | ME-7   | ME-8    | EE-6 | EE-7 | EE-8     | EE-9    | UW-6     | UW-7      | UW-9      | RD-6  | CR-7  | Melanoma | A     | B     | C     |
|---------------|--------|--------|---------|------|------|----------|---------|----------|-----------|-----------|-------|-------|----------|-------|-------|-------|
| M1001_SCF.jpg | -5.48  | -42.46 | -85.19  | 1.80 | 1.93 | 1.17     | 0.71    | -1531.91 | -404.94   | -503.27   | 36.66 | 0.79  | true     | 2     | 0.46  | 21.36 |
| M1002_SCF.jpg | 10.67  | -46.59 | -58.92  | 2.05 | 1.42 | 0.92     | 0.54    | 445.50   | -639.48   | 7572.25   | 12.21 | 0.61  | true     | 2     | 0.38  | 20.33 |
| M1003_SCF.jpg | 1.41   | -21.97 | 38.41   | 1.79 | 1.46 | 0.90     | 0.85    | 15986.99 | -7407.30  | -2592.72  | 75.28 | 0.69  | true     | 2     | 0.47  | 28.07 |
| M1005_SCF.jpg | -5.79  | -7.63  | 78.26   | NaN  | 1.79 | 1.47     | 0.85    | -1962.48 | -3233.70  | 7995.29   | 19.57 | 0.92  | true     | 2     | 0.44  | 17.10 |
| M1006_SCF.jpg | -3.30  | -6.00  | -24.40  | 2.48 | 2.48 | 1.60     | 1.45    | -3657.55 | -7046.21  | 5459.93   | 79.87 | 1.02  | true     | 2     | 0.49  | 18.86 |
| M12_RB.JPG    | 6.57   | 31.69  | 64.11   | NaN  | 1.41 | 1.06     | 0.22    | 2186.89  | 922.68    | 3770.02   | 18.98 | 0.63  | true     | 1     | 0.32  | 25.23 |
| M13_RB.JPG    | -4.84  | 17.81  | -45.64  | NaN  | 1.01 | 0.53     | 0.00    | -353.81  | 284.40    | 0.00      | 3.21  | 0.33  | true     | 3     | 0.21  | 27.12 |
| M1432_RU.jpg  | 17.93  | 56.97  | -67.07  | 1.87 | 1.06 | 1.01     | 0.69    | 1164.82  | 3056.80   | -13127.72 | 44.92 | 0.66  | true     | 2     | 0.55  | 40.84 |
| M15_RB.JPG    | 9.71   | -9.39  | -79.19  | 1.31 | 0.96 | 0.60     | 0.00    | 598.52   | -1765.94  | 0.00      | 9.41  | 0.63  | true     | 1     | 0.24  | 24.93 |
| M17_RB.JPG    | -8.53  | -3.71  | -47.41  | 2.00 | 1.87 | 1.40     | 0.93    | -1741.66 | -21423.72 | 32410.93  | 25.62 | 0.75  | true     | 1     | 0.55  | 29.51 |
| M19_RB.JPG    | 4.49   | -21.48 | -36.77  | 2.09 | 1.58 | 1.40     | 0.88    | 5722.43  | -3669.65  | 14260.27  | 31.04 | 0.71  | true     | 4     | 0.29  | 23.38 |
| M20_RB.JPG    | 14.91  | 27.60  | 35.94   | 1.30 | 1.09 | 0.62     | 0.00    | 1260.00  | 8519.60   | 0.00      | 12.55 | 0.59  | true     | 2     | 0.39  | 16.09 |
| M20_SS.jpg    | 1.83   | -2.14  | -32.32  | NaN  | 2.34 | 1.83     | 0.85    | 12240.37 | -39479.13 | 11513.22  | 42.63 | 1.36  | true     | 5     | 0.51  | 13.57 |
| M22_RB.JPG    | 14.13  | 23.99  | 9.40    | NaN  | 1.39 | 1.21     | 0.39    | 667.99   | 1528.20   | 5011.44   | 7.37  | 0.42  | true     | 3     | 0.57  | 16.04 |
| M22_SS.jpg    | 14.02  | 5.17   | 90.51   | NaN  | 1.04 | 1.03     | 0.48    | 1139.07  | 6126.64   | 9295.50   | 10.49 | 0.53  | true     | 1     | 0.34  | 24.68 |
| M712_SCF.jpg  | -33.42 | -21.65 | 24.12   | 1.21 | 1.78 | 0.97     | 0.61    | -1964.46 | -2656.73  | 30183.99  | 81.60 | 1.77  | true     | 2     | 0.46  | 34.67 |
| M713_SCF.jpg  | 19.52  | 35.06  | 74.29   | 1.47 | 1.12 | 0.82     | 0.83    | 1547.04  | 3038.23   | 48676.02  | 24.39 | 0.49  | true     | 3     | 0.11  | 34.93 |
| M714_SCF.jpg  | 20.70  | -34.46 | 37.65   | 1.87 | 1.88 | 1.04     | 1.70    | 1859.77  | -1910.79  | -3438.46  | 52.33 | 0.96  | true     | 2     | 0.32  | 28.16 |
| M744_SCF.jpg  | 5.37   | 3.69   | -84.49  | 0.89 | 1.12 | 1.23     | 0.47    | 11293.89 | 9546.97   | -1241.97  | 25.11 | 0.67  | true     | 2     | 0.48  | 22.50 |
| M745_SCF.jpg  | -4.84  | 35.96  | -97.38  | 1.64 | 0.94 | 0.56     | 1.12    | -5390.54 | 4414.88   | -3573.68  | 43.30 | 0.70  | true     | 3     | 0.56  | 23.59 |
| M746_SCF.jpg  | 11.70  | 35.42  | 131.84  | 1.80 | 1.46 | 0.90     | 0.98    | 5763.80  | 7031.96   | 24647.87  | 91.15 | 1.07  | true     | 2     | 0.50  | 29.41 |
| M748_SCF.jpg  | -14.98 | 16.54  | -22.25  | 2.00 | 1.56 | 1.78     | 1.86    | -3410.73 | 9979.46   | -8636.59  | 95.75 | 1.20  | true     | 2     | 0.51  | 33.12 |
| M751_SCF.jpg  | -17.21 | -1.29  | 52.92   | 1.60 | 1.53 | 1.09     | 0.05    | -2386.49 | -92750.99 | 759.63    | 28.72 | 0.88  | true     | 2     | 0.50  | 11.58 |
| M752_SCF.jpg  | 3.00   | 9.92   | 39.64   | NaN  | 1.66 | 1.36     | 0.81    | 5077.01  | 6316.90   | 159321.80 | 10.64 | 0.60  | true     | 3     | 0.46  | 31.44 |
| M753_SCF.jpg  | -4.93  | 62.80  | -2.76   | NaN  | 1.24 | 0.74     | 0.18    | -7910.91 | 1291.94   | 2534.24   | 46.86 | 1.09  | true     | 3     | 0.39  | 27.11 |
| N1507_RU.jpg  | -4.30  | 63.43  | -51.67  | 1.59 | 1.02 | 0.98     | 0.56    | -4139.50 | 2435.43   | -104.90   | 17.22 | 0.60  | false    | 2     | 0.18  | 30.70 |
| N4_SS.jpg     | -7.78  | 23.88  | -26.51  | NaN  | 0.79 | 0.58     | 0.00    | -208.06  | 105.82    | 0.00      | 3.45  | 0.39  | false    | 0     | 0.30  | 8.20  |
| N569_RU.jpg   | 6.13   | -1.57  | 17.35   | NaN  | 1.03 | 0.96     | 0.49    | 1026.77  | -7388.71  | 6641.25   | 12.25 | 0.46  | false    | 5     | 0.48  | 11.10 |
| N637_RU.jpg   | 13.78  | -22.28 | -72.71  | 1.37 | 1.27 | 1.18     | 0.20    | 1061.13  | -2343.95  | 3000.65   | 14.37 | 0.41  | false    | 6     | 0.30  | 20.64 |
| N639_RU.jpg   | 18.37  | 40.61  | -27.58  | 1.32 | 0.67 | 0.61     | 0.00    | 404.07   | 1856.27   | 0.00      | 4.68  | 0.34  | false    | 7     | 0.38  | 23.23 |
| N642_RU.jpg   | 10.53  | -36.59 | 55.73   | NaN  | 1.27 | 1.21     | 0.07    | 953.94   | -1200.82  | 2516.11   | 17.63 | 0.66  | false    | 7     | 0.61  | 15.89 |
| M1000_SCF.jpg | -8.08  | 55.21  | -78.91  | 1.49 | 1.11 | 1.33     | 0.54    | -4084.12 | 3702.90   | -2206.76  | 43.53 | 0.90  | true     | 2     | 0.54  | 24.10 |
| M1007_SCF.jpg | 0.73   | 31.90  | 104.91  | 2.15 | 2.11 | 0.99     | 1.17    | 41261.40 | 2745.55   | 8018.60   | 48.34 | 0.88  | true     | 2     | 0.52  | 27.87 |
| M1042_RU.jpg  | -20.88 | 139.26 | 567.46  | 1.54 | 0.99 | 0.25     | 0.00    | -7421.65 | 1382.67   | 0.00      | 34.47 | 1.63  | true     | 2     | 0.12  | 11.96 |
| M716_SCF.jpg  | 5.73   | -2.78  | 83.11   | NaN  | 1.71 | 1.13     | 1.05    | 1995.25  | -17945.72 | 14355.97  | 19.22 | 0.69  | true     | 4     | 0.43  | 19.08 |
| M719_SCF.jpg  | -4.92  | 45.09  | -63.89  | 1.17 | 0.71 | 0.60     | 0.11    | -3023.78 | 3871.47   | -403.34   | 10.06 | 0.29  | true     | 3     | 0.38  | 56.43 |
| M735_SCF.jpg  | -7.62  | 27.10  | -107.58 | NaN  | 1.47 | 1.25     | 0.67    | -1174.20 | 854.15    | 2411.28   | 14.16 | 0.52  | true     | 1     | 0.29  | 26.74 |
| M740_SCF.jpg  | -4.49  | 25.73  | 112.07  | 1.08 | 0.77 | -5863.36 | 2951.77 | 7466.35  | 58.61     | 1.63      | true  | 2     | 0.37     | 32.43 |       |       |
| N647_RU.jpg   | 44.17  | 45.51  | 213.06  | NaN  | 1.37 | 1.27     | 0.64    | 1632.59  | -8515.87  | 51413.58  | 40.50 | 2.23  | false    | 2     | 0.30  | 24.36 |
| N651_RU.jpg   | 10.75  | 14.00  | -26.18  | NaN  | 1.48 | 1.20     | 0.47    | 1534.10  | 4495.08   | 7074.85   | 13.29 | 0.37  | false    | 2     | 0.15  | 14.10 |
| N652_RU.jpg   | 25.18  | 14.28  | -146.12 | 0.68 | 0.00 | 2806.88  | 4309.74 | 0.00     | 23.85     | 0.80      | 0.80  | false | 2        | 0.20  | 10.90 |       |

Sheet1

|              |       |        |         |      |      |      |          |           |           |           |       |       |       |      |       |       |
|--------------|-------|--------|---------|------|------|------|----------|-----------|-----------|-----------|-------|-------|-------|------|-------|-------|
| N654_RU.jpg  | -3.93 | 42.27  | 123.71  | NaN  | 1.32 | 0.96 | 0.56     | -3600.62  | 1422.62   | 12282.36  | 9.41  | 0.38  | false | 2    | 0.32  | 8.14  |
| N659_RU.jpg  | 24.09 | -14.57 | -159.32 | 0.62 | 0.91 | 0.38 | 0.00     | 1960.90   | -3691.68  | 0.00      | 16.81 | 0.51  | false | 2    | 0.31  | 14.97 |
| N715_SCF.jpg | -6.15 | 25.30  | 156.53  | 1.93 | 1.51 | 0.72 | 0.64     | -3435.28  | 1516.84   | -20.55    | 18.81 | 0.61  | false | 2    | 0.62  | 17.81 |
| N854_RU.jpg  | -8.37 | -61.68 | -12.47  | 1.65 | 1.50 | 1.18 | 0.69     | -5145.31  | -2292.73  | 50129.91  | 23.39 | 1.29  | false | 6    | 0.44  | 39.72 |
| N979_RU.jpg  | 8.43  | -24.19 | 91.32   | 1.58 | 1.16 | 0.22 | 0.00     | 518.53    | -1095.84  | 0.00      | 7.36  | 0.39  | false | 4    | 0.39  | 28.11 |
| N10_JL.jpg   | 13.87 | 27.37  | 46.87   | 1.26 | 1.11 | 0.89 | 0.64     | 1398.38   | 2642.20   | -11682.00 | 9.03  | 0.36  | false | 3    | 0.42  | 20.20 |
| N11_JL.jpg   | 1.83  | 30.22  | 47.01   | NaN  | 1.58 | 1.02 | 0.31     | 3802.84   | 612.43    | 3635.61   | 13.39 | 0.49  | false | 16   | 0.33  | 17.21 |
| N12_JL.jpg   | 8.15  | -10.61 | -47.04  | 1.50 | 0.95 | 0.66 | 0.00     | 3002.23   | -17448.25 | -594.90   | 17.18 | 0.92  | false | 2    | 0.52  | 26.19 |
| N15_JL.jpg   | -7.78 | 40.58  | 92.77   | NaN  | 1.65 | 1.11 | 0.53     | -2603.16  | 1593.83   | 8966.04   | 34.90 | 0.88  | false | 7    | 0.28  | 57.77 |
| N16_JL.jpg   | 12.90 | 9.68   | 65.82   | NaN  | 1.88 | 1.60 | 0.86     | 824.70    | 4673.51   | -31325.90 | 18.33 | 0.48  | false | 9    | 0.45  | 19.09 |
| N17_JL.jpg   | 10.09 | -44.10 | -62.28  | 1.68 | 1.59 | 1.33 | 0.93     | 1030.26   | -976.29   | 6046.75   | 30.12 | 0.52  | false | 2    | 0.39  | 18.28 |
| N18_JL.jpg   | -8.92 | 33.48  | -91.02  | 1.26 | 0.81 | 0.00 | -1463.73 | 1163.84   | 0.00      | 6.64      | 0.45  | false | 2     | 0.44 | 22.51 |       |
| N1_JL.jpg    | 0.81  | 49.28  | -89.42  | NaN  | 1.74 | 1.77 | 1.06     | 63500.84  | 4963.68   | 10358.00  | 75.84 | 1.65  | false | 2    | 0.42  | 34.60 |
| N20_JL.jpg   | -3.83 | -39.88 | -84.11  | 1.19 | 0.87 | 1.32 | 0.18     | -4168.52  | -422.56   | -221.70   | 13.86 | 0.49  | false | 2    | 0.57  | 22.97 |
| N21_JL.jpg   | -2.63 | 22.91  | -126.94 | 1.20 | 0.89 | 0.49 | 0.48     | -15952.70 | 4283.56   | -9.172    | 15.76 | 0.58  | false | 1    | 0.54  | 19.86 |
| N22_JL.jpg   | -5.17 | -10.28 | -84.13  | 1.88 | 1.62 | 1.28 | 0.97     | -1211.45  | -833.36   | -2773.14  | 26.77 | 0.65  | false | 10   | 0.40  | 22.56 |
| N23_JL.jpg   | 4.57  | 6.80   | 27.89   | NaN  | 2.09 | 1.39 | 0.81     | -2969.19  | 7402.10   | 16334.42  | 39.98 | 0.99  | false | 4    | 0.47  | 21.25 |
| N2_JL.jpg    | 8.08  | -20.10 | 104.12  | NaN  | 1.30 | 1.10 | 0.83     | 2088.57   | -1614.91  | 8487.03   | 16.97 | 0.55  | false | 2    | 0.47  | 30.32 |
| N4_JL.jpg    | -2.38 | -5.52  | 8.52    | NaN  | 1.98 | 2.13 | 0.69     | -5048.57  | -7387.18  | 10206.82  | 21.71 | 1.08  | false | 7    | 0.36  | 35.39 |
| N5_JL.jpg    | 4.39  | -32.27 | -15.77  | 3.10 | 2.60 | 1.28 | 1.21     | -11510.53 | -6625.46  | 4309.90   | 46.33 | 2.49  | false | 2    | 0.46  | 32.23 |
| N7_JL.jpg    | -5.43 | 25.37  | -100.21 | 1.12 | 0.87 | 0.61 | 0.00     | -3843.84  | 2348.89   | 0.00      | 7.19  | 0.30  | false | 1    | 0.21  | 21.37 |
| N8_JL.jpg    | 10.50 | -31.77 | 97.97   | 1.38 | 1.16 | 0.43 | 0.00     | 424.94    | -1208.95  | 0.00      | 5.87  | 0.30  | false | 3    | 0.49  | 15.09 |
| N9_JL.jpg    | 2.09  | 4.50   | 75.15   | 1.78 | 1.10 | 1.17 | 0.68     | 6642.27   | 24518.51  | -8.91     | 17.94 | 0.64  | false | 2    | 0.43  | 20.19 |
| N25_JL.jpg   | -3.93 | 26.56  | 59.48   | NaN  | 1.43 | 0.83 | 0.58     | -2142.89  | 1308.35   | 9451.71   | 14.99 | 0.42  | false | 0    | 0.26  | 19.72 |
| N26_JL.jpg   | -7.47 | 57.71  | -80.38  | NaN  | 1.02 | 0.61 | 0.00     | -1965.20  | 715.49    | 0.00      | 5.90  | 0.91  | false | 2    | 0.38  | 20.45 |
| N27_JL.jpg   | 16.86 | -29.64 | 54.02   | 1.77 | 1.64 | 1.04 | 0.63     | 831.74    | -1333.77  | -2635.16  | 22.44 | 0.62  | false | 11   | 0.53  | 15.58 |
| N28_JL.jpg   | -3.14 | 16.64  | -35.44  | NaN  | 1.09 | 0.58 | 0.00     | -565.34   | 336.91    | 0.00      | 2.61  | 0.27  | false | 9    | 0.05  | 8.56  |
| N29_JL.jpg   | -6.38 | 17.00  | -120.37 | 1.45 | 0.80 | 0.79 | 0.59     | -2667.09  | 5034.88   | -38.67    | 14.82 | 0.46  | false | 3    | 0.37  | 19.06 |
| N30_JL.jpg   | 2.32  | -48.53 | 6.85    | 1.61 | 1.09 | 0.78 | 0.78     | -355.13   | -24902.41 | 33.78     | 0.84  | 0.31  | false | 8    | 0.31  | 25.90 |